

CFD SIMULATION OF PZT ACTUATED MICROPUMP

Balachandran.C

A Dissertation Submitted to
Indian Institute of Technology Hyderabad
In Partial Fulfillment of the Requirements for
The Degree of Master of Technology



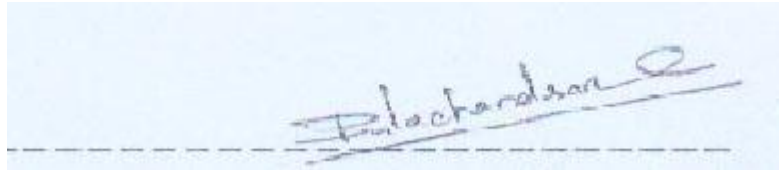
भारतीय प्रौद्योगिकी संस्थान हैदराबाद
Indian Institute of Technology Hyderabad

Department of Mechanical Engineering

July 2011

Declaration

I declare that this written submission represents my ideas in my own words, and where others' ideas or words have been included, I have adequately cited and referenced the original sources. I also declare that I have adhered to all principles of academic honesty and integrity and have not misrepresented or fabricated or falsified any idea/data/fact/source in my submission. I understand that any violation of the above will be a cause for disciplinary action by the Institute and can also evoke penal action from the sources that have thus not been properly cited, or from whom proper permission has not been taken when needed.

A photograph of a handwritten signature in blue ink on a light blue background. The signature is written in cursive and appears to be 'Balachandran.C'. Below the signature is a dashed horizontal line.

Balachandran.C

me09g003

Approval Sheet

This thesis entitled “CFD Simulation of PZT Actuated Micropump” by Balachandran.C is approved for the degree of Master of Technology from IIT Hyderabad.



Dr. Kirti Chandra Sahu

(Examiner)

Assistant Professor

Department of Chemical Engineering



Dr. Abhay Sharma

(Examiner)

Assistant Professor

Department of Mechanical Engineering



Dr. Raja Banerjee

(Advisor)

Assistant Professor

Department of Mechanical Engineering

Dr. Saptarshi Majumdar

(Chairman)

Assistant Professor

Department of Chemical Engineering

Acknowledgements

Develop an attitude of gratitude, and give thanks for everything that happens to you, knowing that every step forward is a step toward achieving something bigger and better than your current situation. This thesis is the result of work whereby I have been accompanied and supported by many people. It is a pleasant aspect that I have now the opportunity to express my gratitude for all of them. With immense pleasure I express my deep and sincere gratitude, regards and thanks to my thesis advisor Dr. Raja Banerjee for his excellent guidance, invaluable suggestions and continuous encouragement at all the stages of my research work. His wide knowledge and logical way of thinking have been of great value for me. As a guide he has a great influence on me, both as a person and as a professional. I would like to acknowledge my co-guide Dr. Ashok Pandey who gave inputs, moment where turning point of thesis occurred. I would also like to thank all the staff members and my colleagues for their inspiration and friendship making the life at IIT Hyderabad memorable. Above all, I am blessed with such caring parents. I extend my deepest gratitude to my parents and my elder brother C. Satheesh Chandran for their affection, encouragement and support. Thank you very much.

Dedicated

to

My Parents

Abstract

Micropumps with various types of actuations have been using in microfluidic transport for liquid drug delivery. Due to the complexity of the flow field, particle transport through a valve less micropump might be challenging in comparison to a pressure-driven flow micropumps. In order to understand better and develop an optimized model for the delivery of drug particles through valve less micropumps, computational simulations may be required. In this thesis, fluid flow through valve less micropump is simulated through 2-D computational fluid dynamics combined with VOF multiphase model.

After computational validation, the effects of actuation frequency, actuation pressure, nozzle diameter, viscosity, surface tension and transporting channel on the pump flow have been investigated. Out of which, nozzle diameter, frequency, pressure plays prominent role in size and shape of droplet formation.

Optimum micro pump design has been created along with the Piezo electric circuit which drives the valve less micro pump. The micropump developed operates in high frequency range (100 kHz - 250 kHz) and under moderate pressure (60kPa). The computational analysis results presented demonstrate that it is possible to optimize the proposed valveless micropump design through numerical simulations for specific delivery of drug particles.

Nomenclature

Description	symbol	Description	symbol
Diaphragm area	A_d	Maximum volumetric flow rate	Q_{max}
Magnetic flux density	B	Reynolds number	R
Capacitance	C	Package size	S_p
Diaphragm diameter	d_d	Strouhal number	S_r
Material Young's modulus	E_y	Stress	σ
Compression ratio	ε_c	Material yield stress	σ_y
Thermodynamic efficiency	η	Diaphragm thickness	t_d
Estimated thermodynamic efficiency	η_{est}	Flow velocity	U
Self-pumping frequency	f_{sp}	Electrical potential difference	V
Diaphragm resonant frequency	f_r	Dead volume	V_o
Operating frequency	f	Stoke Volume	ΔV
Compressibility	k	Diaphragm centreline displacement	y_o
Viscosity	μ	Density	ρ
Material Poisson ratio	ν	Coefficient of Thermal expansion	β
Applied driver pressure	p_a	Diaphragm radius	a
Pressure differential	Δp	Maximum pressure differential	Δp_{max}

List of figures

Fig 1.1: Classification of micropumps	2
Fig 1.2: Piezoelectric driver in lateral/axial configurations	4
Fig 1.3: Schematic of heater thermo-pneumatic actuation pump.....	5
Fig 1.4: Schematic of electric actuation micropump.....	6
Fig 1.5: Typical working of pneumatic pump.....	6
Fig 1.6: Operational principle of pump with flaps	7
Fig 1.7: Typical single chamber micropump model	8
Fig 1.8: Multiple chamber micropump(series)	8
Fig 1.9: Multiple chamber micropump(parallel).....	9
Fig 1.10: Micro gear pumps operating principle.....	10
Fig 1.11: Centrifugal micropump.....	11
Fig 1.12: Cross sectional view of impeller.....	11
Fig 1.13: Surface acoustic micropump.....	12
Fig 1.14: Electrochemistry of a solid liquid interface and Electroosmotic flow	14
Fig 1.15 Magneto-hydrodynamic micropump	15
Fig 1.16: Jet break up regimes.....	17
Fig 1.17: Schematic diagram of the jet breakup length curve.....	18
Fig 1.18: Typical working of Piezo electric actuated micropump.....	20
Fig 1.19 Piezoelectric transducer operation lateral.....	24
Fig 1.20: Schematic of DoD and MDG pump chamber and dimensions.....	30
Fig 1.21: Exploded view of proposed micropump	31
Fig 1.22: Schematic cross-section of the piezoelectric micropump with a close-up of the valve geometry	32
Fig 1.23: Critical parameters and dimensions of proposed micropump	33
Fig 1.24: Sketch of micropump cross-section	34
Fig 2.1: Schematic of membrane deflection.....	37
Fig 2.2: Voltage supply circuit of PZT	43
Fig 3.1: Meshed domain of micropump created on Altair-Hypermesh.....	44

Fig 3.2: Measuring contact angle.....	54
Fig 3.3: Initial patched domain.....	54
Fig 3.4: Micropump mesh.....	55
Fig 3.5: Motion transfer from PZT to membrane.....	55
Fig 4.1: Plots of velocity at interface for various meshes.....	59
Fig 4.2: Bar chart comparison for Interface velocity.....	60
Fig 4.3: Plots of static pressure at inlet for various meshes.....	60
Fig 4.4: Bar chart comparison of static pressure for various meshes.....	61
Fig 4.5: Bar chart comparison of average droplet velocity for various meshes ...	61
Fig 4.6: Surface to Volume ratio for different meshes at $50\mu s$	62
Fig 4.7: Jet break up in micropump.....	63
Fig 4.8: Instant of a breaking of jet.....	65
Fig 4.9: Micropump droplet dispersion (base case).....	66
Fig 4.10: Effect of frequency on droplet dispersion.....	67
Fig 4.11: Plot of Droplet Velocity Vs frequency of actuation.....	67
Fig 4.12: Plot of volume flow rate Vs frequency.....	68
Fig 4.13: Effect of Nozzle diameter on droplet dispersion.....	68
Fig 4.14: Effect of pressure on droplet dispersion.....	69
Fig 4.15: Effect of viscosity on droplet dispersion.....	70
Fig 4.16: Effect of surface tension on droplet dispersion.....	71
Fig 4.17: Effect of contact angle on droplet dispersion.....	72
Fig 4.18: Different meshes with various fillet radii.....	73
Fig 4.19: Change in surface to volume ratio for a droplet through spray domain.....	74
Fig 4.20: Contours of pressure over successive cycles.....	75
Fig 4.21: Imposing electrostatic charge on micropump spray domain.....	77

List of Tables

Table 1.1: Some of the mechanical micropumps reported.....	26
Table 3.1: Dimensions of the micropump.....	45
Table 3.2: Quality parameter values of the mesh (converged).....	45
Table 4.1: Mesh grid info	58
Table 4.2: Mesh quality info.....	58
Table 4.3: Fluid properties used in simulation	62
Table 4.4: Variation of average droplet velocity with nozzle diameter.....	69
Table 4.5: Shows the maximum and minimum values of pressure attained over cycles.	75

Contents

Declaration	
Approval Sheet	
Acknowledgements.....	
Abstract.....	
Nomenclature	iv
1 Introduction	1
1.1 Back ground.....	1
1.2 Classification of micropump	1
1.2.1 Mechanical pumps	3
1.2.1.1.Displacement pumps.....	3
1.2.1.1.1Diaphragm pumps.....	3
a.Piezoactuated.....	3
b.Thermo pneumatic.....	5
c.Electrostatic.....	5
d.Pneumatic	6
1.2.1.1.2 Classificatio based on valves	6
a.Flap	6
b.Fixed -geometry	7
c.Nozzle-diffuser	7
d.Tesla.....	7
1.2.1.1.3Classification based on chambers	8
a.Single.....	8
b.Multiple/series(peristaltic).....	8
c.Multiple/parallel.....	9
1.2.1.1.4Aperiodic displacement mechanical pumps.....	9
a.Pneumatic	9
1.2.1.1.5 Rotary pumps.....	10
1.2.1.1.Dynamic pumps	10
1.2.1.2.1 Centrifugal pumps	11

1.2.1.2.2 Ultrasonic pumps.....	12
1.2.1 Non mechanical pumps	13
1.2.2.1 Phase change/thermal.....	13
1.2.2.2 Electro-capillary	13
1.2.2.3 Electro-wetting.....	13
1.2.2.4 Electro hydrodynamic pumps	13
1.2.2.5 Electroosmotic pumps	13
1.2.2.6 Magneto-hydrodynamic pump	15
1.3 Significance of mechanical micropump	15
1.4 Break up Regimes.....	16
1.4.1 Breaking of jet	18
1.4.2 Mechanism of jet breakup.....	19
1.4.3 Theoretical droplet size calculation	19
1.5 Concept and Design of micropump	19
1.6 Literature Survey.....	20
1.6.1 Modeling reciprocating displacement micropump operation	21
1.6.2 Works on chamber configuration	22
1.6.3 Materials and fabrication techniques	23
1.6.4 Drivers	24
1.6.5 Reported micropumps.....	26
1.6.6 Miscellaneous works.....	28
1.7 Challenged and Limitations.....	35
1.2 Objective	35
2 Theory	36
Mathematical modeling	
1.2 Deflection models	38
2.1.1 Analysis of small deflection Diaphragm	38
2.1.2 Analysis of medium deflection Diaphragm.....	38
2.1.3 Analysis of large deflection Diaphragm	39
2.2 Modelling the diaphragm.....	40

2.3 Design parameters of micropump.....	40
2.4 Compressibility and theoretical discharge.....	42
2.5 Design of Voltage circuit for PZT.....	43
3 Numerical procedure	44
3.1 Meshing	44
3.1.1 Dimensions	44
3.1.2 Meshing Procedure	44
3.2 Simulation	45
3.3 VOF	46
3.3.1 Transient VOF calculations.....	46
3.4 Volume fraction equations	47
3.5 Schemes used for simulation.....	47
3.5.1 Implicit schemes.....	47
3.6 Material properties	48
3.7 Solution methods.....	48
3.7.1 PISO.....	48
3.7.2 Green Gauss Cell based Method.....	49
3.7.3 Body weighted force.....	49
3.7.4 Second order upwind scheme.....	49
3.7.5 The geometric reconstruction scheme	50
3.8 Momentum equation	50
3.9 Surface Tension and wall adhesion.....	51
3.9.1 Surface Tension.....	53
3.9.1.1 When Surface Tension effects are important	53
3.9.2 Wall adhesion	53
3.10 Problem setup	54
3.10.1 Initialization.....	54
3.10.2 Grid Information.....	55
3.10.3 Model setup	55
3.10.4 Boundary condition	55
3.10.5 Solution setup.....	55
3.10.6 CFD Analysis	56
3.10.7 Membrane motion.....	57
3.11 User defined functions.....	57

4 Results	58
4.1 Grid Independency	58
4.1.1 Parameters compared for grid independency.....	59
4.1.1.1 Velocity at Interface	59
4.1.1.2 Static pressure at inlet	60
4.1.1.3 Velocity of droplet	61
4.1.1.4 Surface to Volume ratio	62
4.2 Theoretical validation	63
4.2.1 Determination of jet regime	63
4.2.2 Determination of droplet size.....	64
4.2.3 Determination of wavelength of disturbance.....	65
4.3 Micropump droplet dispersion of base case	66
4.3.1 Effect of frequency.....	67
4.3.2 Effect of diameter	68
4.3.1 Effect of pressure.....	69
4.3.1 Effect of viscosity.....	70
4.3.1 Effect of surface tension.....	71
4.3.1 Effect of contact angle.....	72
4.3.1 Effect of fillet.....	73
4.4 Hydrodynamic resistance.....	74
4.5 Contours of pressure over successive cycles.....	75
5 Conclusion and Scope of future works	76
Appendix	78
Reference	81

Chapter 1

Introduction

1.1 Back ground

Since the invention of first micropump is 1980, a lot of mechanical and non-mechanical pumps have been reported with different types of actuations, each having its own capabilities and limits. The necessity of micropump has been significant for biomedical systems especially in drug delivery systems. As micropump deals with discharge of order of microliters and different sources of electric powers used for its functioning, it came under core research area of MEMS. Research has been going on to find an easiest method to operate the micropump in perspective of its actuation.

Many designs have been reported with single to multi chambers to deliver droplets of order of nano to microliters. This would be a tedious task to find a proper way of control of micropumps and type of actuation, unless we know the factors influencing jet break up, the effect of actuation parameters and fluid properties on the droplet discharge.

1.2 Classification of Micropumps

Micropumps generally classified into two categories

- Mechanical Pumps
- Non mechanical pumps

Mechanical Pumps, which uses mechanical energy or moving boundary to add momentum to the fluid or gas.

Non mechanical Pumps add momentum to the fluid by converting non-mechanical energy into kinetic energy [1].

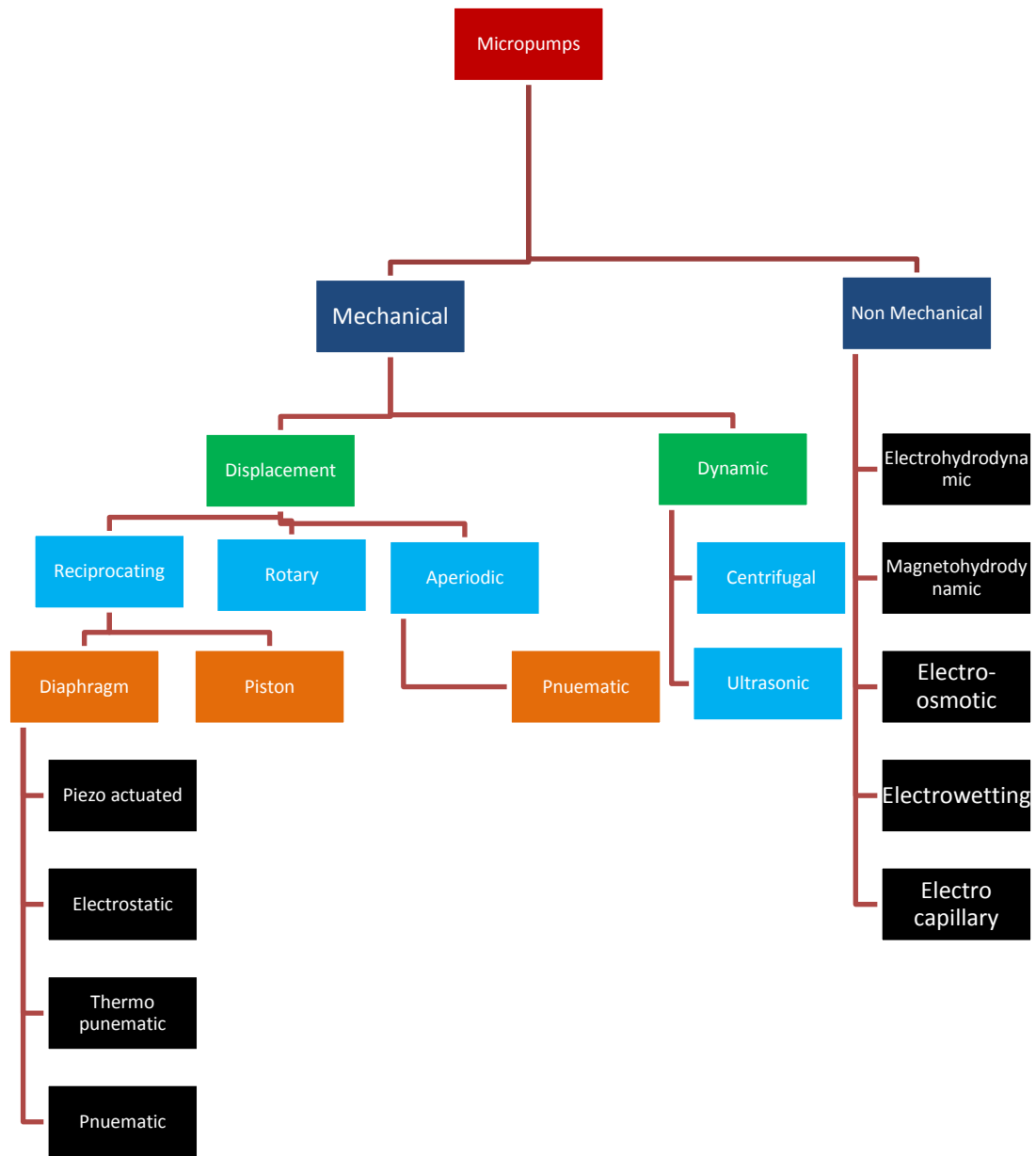


Figure 1.1: Classification of micropumps [2]

1.2.1 Mechanical Pumps

Mechanical Pumps can be classified into

- Displacement pumps and
- Dynamic pumps

1.2.1.1 Displacement pumps

Many displacement pumps operate in a periodic manner, incorporating some means of rectifying periodic fluid motion to produce net flow. Such periodic displacement pumps can be further broken down into pumps that are based on reciprocating motion, as of a piston or a diaphragm, and pumps that are based on rotary elements such as gears or vanes [3].

The majority of micropumps are reciprocating displacement pumps in which the moving surface is a diaphragm. These are sometimes called membrane pumps or diaphragm pumps. During operation, the driver acts on the pump diaphragm to alternately increase and decrease the pump chamber volume. Fluid is drawn into the pump chamber during the chamber expansion/suction stroke and forced out of the pump chamber during the contraction/discharge stroke. The check valves at the inlet and outlet are oriented to favour flow into and out of the pump chamber, respectively, rectifying the flow over a two-stroke pump cycle. Diaphragm pumps are broadly classified into following based on the drivers.

1.2.1.1.1 Diaphragm pumps

Classification based on drivers

a) Piezo actuated

These are diaphragm pumps which work on the Piezo Electric Transducer as source of actuation. Piezoelectric mechanism is the most widely used in reciprocating pumps and grown to be the dominant in drug delivery and biomedical applications. It involves strain induced by an applied electric field on an piezoelectric crystal. The piezoelectric effect is related to coupling that exists between mechanical deformation and electrical polarization.

$$\varepsilon = s^E \sigma + dE \quad (1.1)$$

Where s^E is the compliance tensor and σ is the stress, d is the piezoelectric charge constant tensor and E is the electric field. When used in micropumps, the basic idea is to convert the transverse piezoelectric strain to a large bending displacement in the perpendicular direction.

In most implementations, strain in the piezoelectric layer is induced by either d_{31} or d_{33} piezoelectric coupling. In d_{31} mode, a transverse strain (perpendicular to the polarization axis) is caused by the piezoelectric coupling while the d_{33} mode induces a strain parallel to the polarization [1].

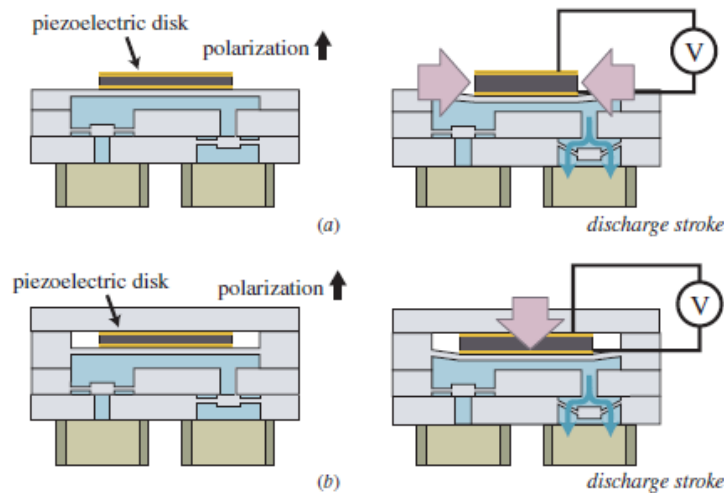


Figure 1.2 (a) Piezo electric driver in the lateral-strain configuration. The bottom surface of the piezoelectric disk is bonded to the pump diaphragm the top surface is unconstrained. During operation, the pump diaphragm deflects under a bending moment produced by radial strain in the piezoelectric disk. An axial electric field is applied to the disk. (b) Piezoelectric driver in the axial-strain configuration, where a piezoelectric disk is mounted between the pump diaphragm and a rigid frame. During operation, the pump diaphragm deflects primarily as a result of axial strain in the piezoelectric disk. As in (a), an axial electric field is applied to the disk [1].

Voltage induced deflection of the membrane will cause the volume of liquid in the chamber to change. When AC voltage is applied, the membrane will move up and down alternately to complete expansion and contraction modes. The two different excitation modes, transverse strain and axial-strain, are illustrated in Figs 1.2. (a) and (b). In Fig 1.2 (a), the bottom surface of the piezoelectric actuator is directly bonded to the membrane of the micropump, while the top surface of it is unconstrained. During operation, an axial electric field is applied to the piezoelectric actuator. The pump membrane deflects in a radial direction under a bending moment causing the upward and downward movement.

In Fig 1.2 (b), the piezoelectric actuator is positioned on the surface of the membrane and the top is constrained on a rigid frame. The pump diaphragm generates a large vertical force and consequently a large vertical displacement as a result of axial-strain of the piezoelectric actuator when voltage is applied.

b) Thermo pneumatic

Thermal actuation mechanism includes thermal expansion and phase change types. Some popular thermally induced micropumps usually take the forms of thermo-pneumatic, shape memory alloys or bimetallic actuation methods. Representative thermal actuation micropumps, such as single gas expansion, liquid-gas phase change (vaporization and condensation) and two solid-phase change are briefly introduced here in [3].

Thermo pneumatic driver, in which a thin-film resistive element heats the driver working fluid in a secondary chamber above the pump chamber. The heated fluid expands, exerting pressure on the pump diaphragm as in fig 3.

Generally, a thermo-pneumatic actuator consists of a heater, diaphragm and a sealing cavity shown in Fig 3. It is based on the thermally induced volume change or phase change of fluids sealed in a chamber. The periodical change in volume of the chamber results in a pressure change inside the cavity to actuate the flexible diaphragm.

For the liquid, the pressure change is expressed as:

$$\Delta P = E \left(\beta \Delta T - \frac{\Delta V}{V} \right) \quad (1.2)$$

Where ΔP is the pressure difference; E is the modulus of elasticity; β is the thermal expansion coefficient; ΔT the temperature increase and $\frac{\Delta V}{V}$ is the volume change percentage.

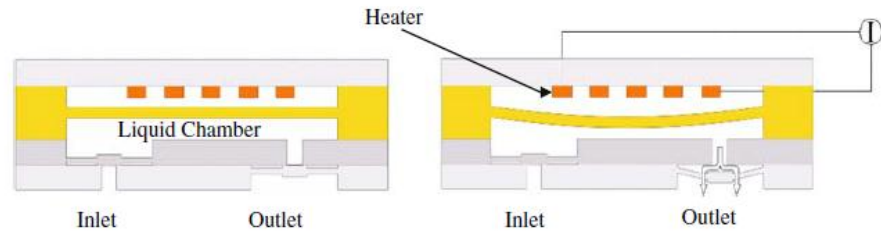


Fig1.3(c) Schematic of Heater thermo-pneumatic actuation micropump [4]

c) Electrostatic

Electrostatic driver, in which the pump diaphragm deflects upward when an electric potential difference is applied between parallel electrodes. Electrostatically driven reciprocating displacement micropumps typically have a powered suction stroke and an unpowered discharge stroke as in fig 1.4. Dielectric coatings are used to prevent shorting. Major limitations of

Electrostatic micropumps are less deflection upto $5\mu m$ with applied actuation voltage around 200V [1].

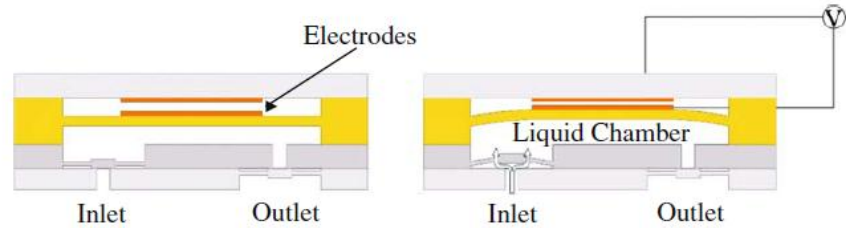


Figure 1.4: Schematic of electrostatic actuation micropump [4]

Electrostatic actuation depends on the columbic attraction of oppositely charged material bodies to induce displacement or exert force. The attraction force can be calculated from the stored energy in the electrostatic field of the device. When a voltage V is applied between two plates of area A separated by an air gap d , the electrostatic force can be described as follows

$$F = \frac{\epsilon_0 AV^2}{2d^2} \quad (1.3)$$

where ϵ_0 is the permittivity of free space.

d) Pneumatic

External pneumatic driver, in which active valves alternately pressurize and vent a secondary chamber above the pump diaphragm as in fig 1.5

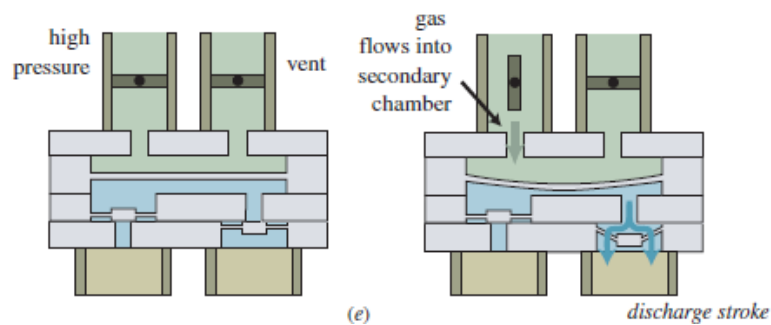


Fig 1.5 shows the typical working of pneumatic pump [1]

1.2.1.1.2 Classification based on valves

a) Flap

The performance of check valves at the inlet and outlet of the pump chamber is critical to the operation of reciprocating displacement micropumps. Microvalves have been reviewed recently [6, 7]. Figures of merit for check valves include diodicity, or the ratio between the forward and reverse pressure drop across the valve, maximum operating pressure, ease of fabrication and

reliability. Most micropumps incorporate some sort of normally closed, passive (non-actuated), mechanical flap structure. In case of active valves, valves are opened and closed by an actuating force offer improved performance at the expense of fabrication and operational complexity.

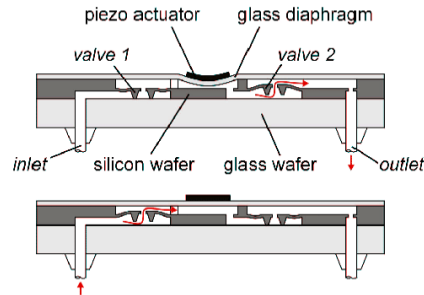


Figure 1.6: Operational principle of pump with flaps [3]

b) Fixed- geometry

In fixed – geometry, there would not be any moving structure. In fixed-geometry valves may be advantageous when the working fluid contains cells or other materials prone to damage or clogging [8].

c) Nozzle- diffuser

The operational principle of the micropump is based on the flow characteristic difference between the nozzle and the diffuser. Inlet and outlet alternatively act as nozzle and diffuser for supply and pumping modes based on flow rate. The flow channels at the inlet and the outlet are designed to give different flow resistance in the forward and reverse directions [9].

The flow rate is
$$Q = 2\Delta Vf \frac{\sqrt{n}-1}{\sqrt{n}+1} \quad (1.4)$$

Where n is $\frac{\epsilon_{reverse}}{\epsilon_{forward}}$

d) Tesla

A Tesla valve is a valve allowing for a fluid to flow very preferentially (or entirely) in one direction, but without the moving parts usually found in valves. The principle is that currents flow along different paths in different directions, and that these differences have a disproportionate effect on the resistance of the valve [10].

1.2.1.1.3 Classification based on chambers

a) Single

Pumping having a single fluid chamber for its operation.

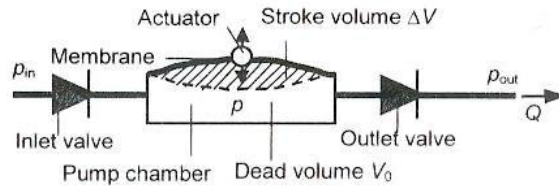


Fig 1.7: typical single chamber micropump model [3]

b) Multiple/series (peristaltic)

These are pumps having more than one chamber connected in parallel or series based on discharge or pressure requirements as in fig below.

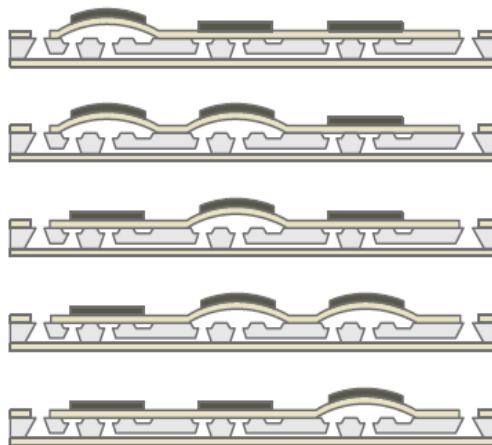


Figure 1.8: The micropump is made from an etched silicon substrate bonded between two glass plates. Piezoelectric disks are bonded to the glass above each of the three pump chambers etched in the silicon. Applying a voltage to a piezoelectric actuator causes the glass to bow away from the pump chamber beneath, drawing in fluid. Staggered actuation as shown results in net fluid flow from the inlet at left to the outlet at right [1].

The pumping concept is based on the peristaltic motion of the pump chambers. Theoretically, peristaltic pumps should have three or more pump chambers with reciprocating membranes.

c) Multiple/Parallel

The diffuser pump delivers a pulsating or periodic flow. To reduce this phenomenon, two pump chambers have been connected in parallel and working in an opposite phase. Theoretically, this will also double the pump flow compared to a single chamber pump.

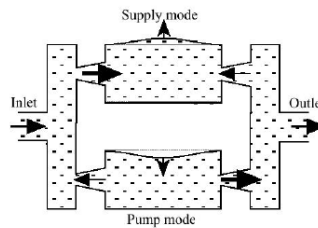


Fig 1.9: Operation of a multiple –parallel micropump

1.2.1.1.4 Aperiodic displacement mechanical pumps

In aperiodic displacement pumps, the operation of which does not inherently depend on periodic movement of the pressure-exerting boundary. Aperiodic displacement pumps typically pump only a limited volume of working fluid; a syringe pump is a common macroscale example. Following are different aperiodic displacement pump types based on its driver source.

a) Pneumatic

Pneumatically driven aperiodic displacement pumping is readily implemented at the micro scale. Interfacial tension effects often take the place of traditional moving surfaces for applying pressure on the working fluid [11]. These are pumps having aperiodic displacement micropump based on injecting bubbles into a micro channel through a port midway along its length. Axial variations in surface tension due to discontinuities in the micro-channel height produce net flow.

1.2.1.1.5 Rotary Pumps

In macro world, rotary pumps are suitable for pumping highly viscous fluids. Main requirement for rotary pumps are

- Strong external actuators
- Fully integrated actuators are impractical
- Size tends to be large

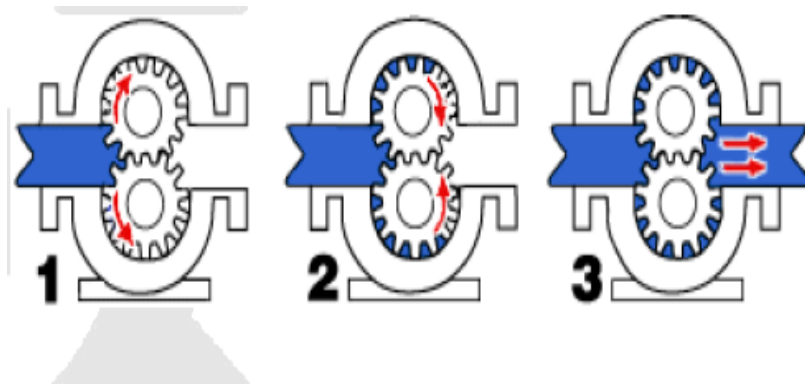


Fig 1.10: Micro gear pumps- operating principle [3].

1.2.1.2 Dynamic Pumps

Dynamic pumps include centrifugal pumps, which are typically ineffective at low Reynolds numbers and have only been miniaturized to a limited extent, as well as pumps in which an electromagnetic field interacts directly with the working fluid to produce pressure and flow (electrohydrodynamic pumps, electro-osmotic pumps and magneto hydrodynamic pumps) and acoustic-wave micropumps [2].

Dynamic pumps are broadly classified into

- Centrifugal
- Ultrasonic

1.2.1.2.1 Centrifugal Pumps

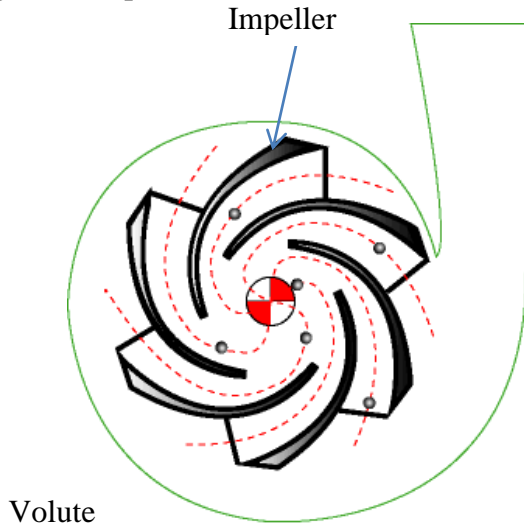


Figure 1.11: Centrifugal Pump [3]

The impeller produces liquid velocity and the volute forces the liquid to discharge from the pump converting velocity to pressure. Because of the high viscosity and the small radius of the rotor centrifugal pumps with internal actuators have not been powerful enough to drive liquids in micro channels. The flow velocity is controlled by the angular velocity of the disc. At the channel exit, the liquid will proceed if the centrifugal force F_C is larger than the capillary force F_S .

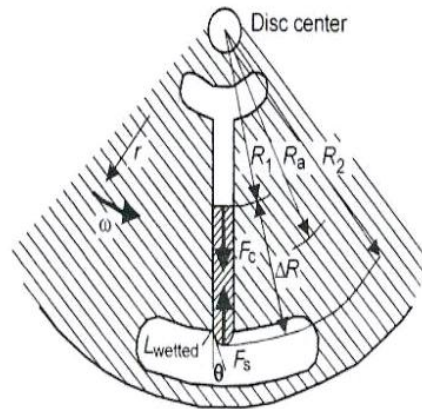


Figure 1.12: Cross sectional view of impeller [2-3]

$$\frac{dF_C}{dr} = \rho \omega^2 r$$

$$F_S = \frac{\sigma \cos\theta L_{wetted}}{A}$$

Where σ is surface tension, θ , is contact angle, L_{wetted} is wetted perimeter of the channel, A is the channel area.

1.2.1.2.2 Ultrasonic pumps

The pumping effect is caused by acoustic streaming which is induced by mechanical travelling wave like

- flexural plate wave
- surface acoustic wave

Wave is excited by interdigital transducers placed on a thin membrane coated with piezoelectric film. Surface acoustic wave causes an elliptical motion of the fluid near the wall.

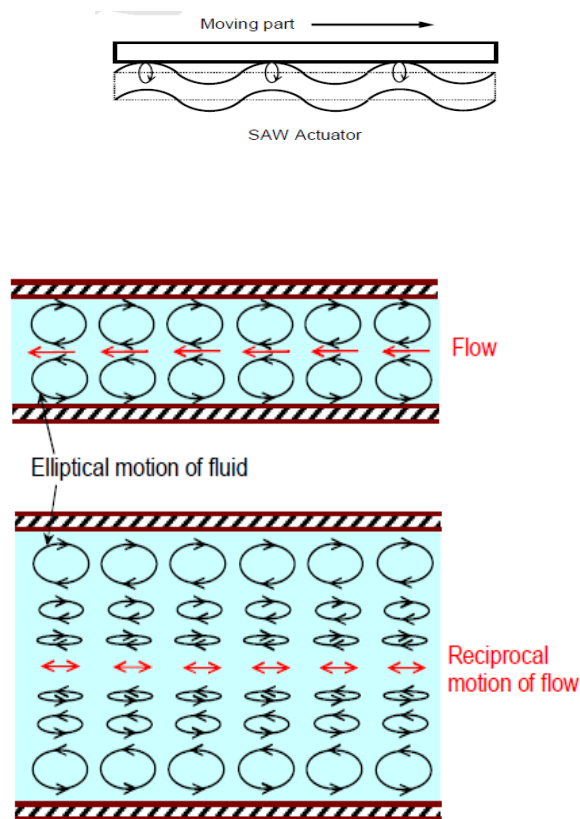


Fig 1.13: Surface Acoustic micropump

The elliptic motion decreases along the radius from the channel wall to the centre. If the channel diameter is large compared to the amplitude of the wave, fluid cannot be pumped due to the reciprocating motion at the centre of the channel.

1.2.2 Non Mechanical Pumps

They can be classified into

1.2.2.1 Phase change/Thermal

These are aperiodic displacement micropumps based on thermal or electrochemical phase change. Here pump works on thermal gradient as when the liquid is boiled locally at the close end micro channels. Sometimes it uses arrays of heating elements to generate flow in channels open on both ends.

1.2.2.2 Electro-capillary

Here fluids are set into motion by changing the Interfacial surface tension. This is achieved by applying potential at the channel ends.

1.2.2.3 Electro-wetting

The electro-wetting effect has been defined as "the change in solid-electrolyte contact angle due to an applied potential difference between the solid and the electrolyte". The fringing field at the corners of the electrolyte droplet tend to pull the droplet down onto the electrode, lowering the macroscopic contact angle and increasing the droplet contact area.

1.2.2.4 Electro hydrodynamic Pumps

Electrohydrodynamic micropumps are based on the interaction of electrostatic forces with ions in dielectric fluids [13]. The electric body force density F_e that results from an applied electric field with magnitude E is given by

$$F_e = qE + P \cdot \nabla E - \frac{1}{2} E^2 \nabla \epsilon + \frac{1}{2} \nabla [E^2 \left(\frac{\partial \epsilon}{\partial \rho} \right) T \rho] \quad (1.5)$$

where q is the charge density, ϵ is the fluid permittivity, ρ is the fluid density, T is the fluid temperature and P is the polarization vector.

1.2.2.5 Electroosmotic Pumps

Electroosmotic (EO) pumping leverages the surface charge that spontaneously develops when a liquid comes in contact with a solid [5-7]. Bulk liquid counter-ions shield this surface charge, completing the so-called electrical double layer (EDL). The characteristic thickness of the electric double layers the Debye shielding length, λ_D , of the ionic solution, given by

$$\lambda_D = \left[\frac{\epsilon k T}{e^2 \sum_i z_i n_{\infty, i}} \right]^{\frac{1}{2}} \quad (1.6)$$

Here ϵ and T are the electrical permittivity and temperature of the solution, respectively; z_i and n_∞ are the valence number and number density, respectively, of the ionic species i in solution; k is the Boltzmann constant; and e is the electron charge. Some portion of the counter-ions in the liquid phase of the EDL can be set into motion by applying an electric field parallel to the wall. The mobile ions drag bulk liquid in the direction of the electric force.

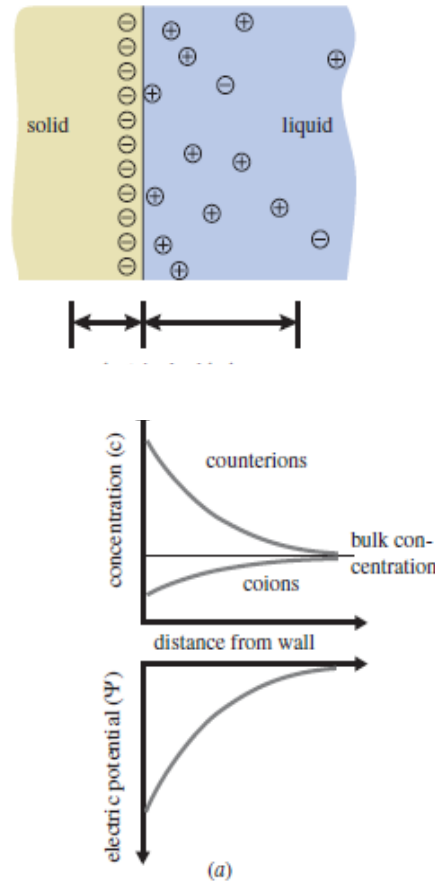
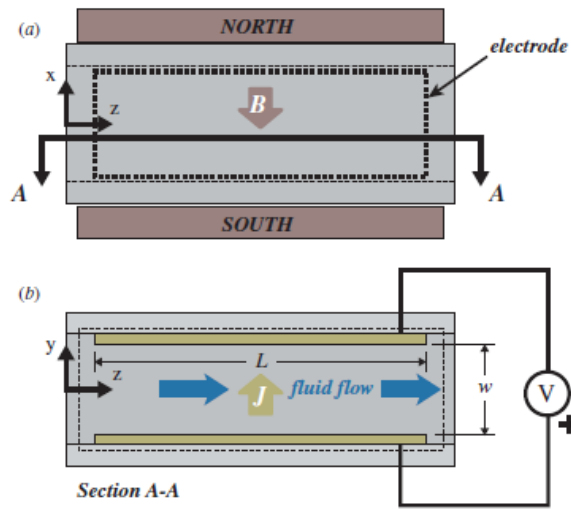


Fig 1.14. Electrochemistry of a solid–liquid interface and electroosmotic flow. (a) Chemical reactions at the interface leave the surface charged (shown as negative here). Counter ions in the liquid accumulate in the vicinity of the charged surface, forming the electric double layer. (b) An externally applied electric field causes motion of counter ions that shield a negative wall charge. Ion drag forces the flow against a pressure gradient [7].

1.2.2.6 Magneto-hydrodynamic pumps

Magneto-hydrodynamic micropumps are pumps in which current-carrying ions in aqueous solutions are subjected to a magnetic field to impart a Lorentz force on the liquid and induce flow [16]. In a rectangular channel with transverse current density J_y and perpendicular transverse magnetic flux density B_x , the maximum pressure is

$$P_{max,MHD,th} = J_y B_x l \quad (1.7)$$



Top view fig1.15 (a) and section view fig 15(b) schematics of a simple magneto hydrodynamic micropump. A transverse magnetic field exerts a Lorentz force ($F = J \times B_w$) on current-carrying ions flowing across the channel, producing flow in the axial direction [8].

1.3 Significance of mechanical pumping methods

Since in micropumps, dimensions are of order of $100\mu m$, capillary force comes into a major picture particularly in hydrophilic channels and porous materials, same force can drive the fluids. But Passive liquid propulsion using capillary forces cannot be actively influenced any more when the process has started [3]. Active pumping technologies facilitate stopping, re-starting, reversing, altering flow rates and flow rate ratios, which can be done only with mechanical and non-mechanical pumping methods. But mechanical pumping method differs from non-mechanical in following aspects.

Mechanical pumping gives

- High output pressure (Except for oscillation pumping).
- Broad range of flow velocities.
- Insensitivity to the fluid nature.
- It can pump different fluids including liquid and gas.

In mechanical pump PZT itself differs from other pumping methods like

- Better control over diaphragm motion;
- Better interface to electronic circuits;
- Less response time
- Voltage requirement is high, but power consumption is low

It is very important to study about breaking up of jet into drops in micropump as here volume of each satellite drop is significant.

1.4 Break up Regimes

The breakup of a liquid jet injected through a circular nozzle hole into a stagnant gas has been studied frequently. Previous studies have established that the spray properties are influenced by an unusually large number of parameters, including nozzle internal flow effects resulting from cavitation, the jet velocity profile and turbulence at the nozzle exit, and the physical and thermodynamic states of both liquid and gas. The precise mechanisms of breakup are still being researched [9]. However, linear stability theory can provide qualitative descriptions of breakup phenomena and predict the existence of various breakup regimes. It is noteworthy that the influence of nozzle internal flow effects is included only empirically in most jet breakup theories. These effects are known to be important, particularly for high-speed jet breakup.

Jet breakup phenomena have been divided into regimes that reflect differences in the appearance of jets as the operating conditions are changed. The regimes are due to the action of dominant forces on the jet, leading to its breakup, and it is important that these forces be identified in order to explain the breakup mechanism in each regime. The case of a round liquid jet injected into a stagnant gas is shown in Figure 1[3]. Four main breakup regimes have been identified that correspond to different combinations of liquid inertia, surface tension, and aerodynamic forces acting on the jet. These have been named the Rayleigh regime, the first wind-induced regime, the second wind-induced regime, and the atomization regime.

Drop sizes much smaller than the jet diameter. Breakup starts at nozzle exit. At low jet velocities, the growth of long-wavelength, small-amplitude disturbances on the liquid surface promoted by the interaction between the liquid and ambient gas is believed to initiate the liquid breakup process. The existence of these waves is clearly demonstrated in Figure 1*a* and *b*. For high-speed liquid jets, the breakup is thought to result from the unstable growth of short wavelength waves (Figure 1*c* and *d*). The breakup drop sizes are on the order of the jet diameter in the Rayleigh and first wind-induced regimes. The drop sizes are very much less than the jet diameter in the second wind-induced and atomization regimes.

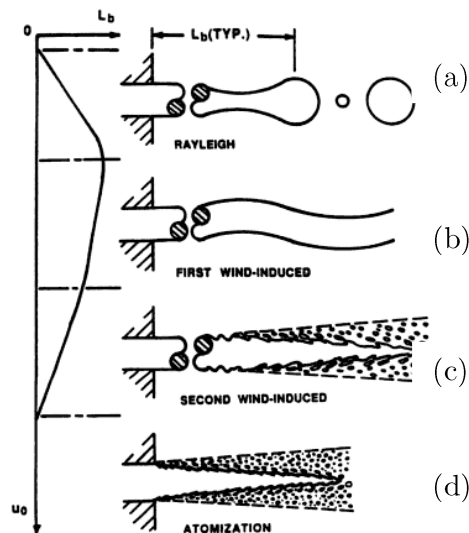


Figure 1.16 (a) Rayleigh breakup. Drop diameters larger than the jet diameter. Breakup occurs many nozzle diameters downstream of nozzle. (b) First wind-induced regime. Drops with diameters of the order of jet diameter. Breakup occurs many nozzle diameters downstream of nozzle. (c) Second wind-induced regime. Drop sizes smaller than the jet diameter. Breakup starts some distance downstream of nozzle. (d) Atomization regime [9].

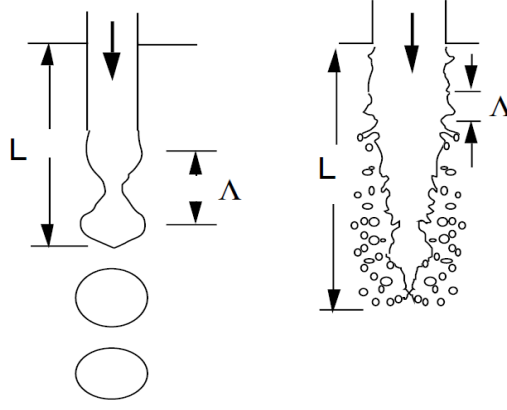


Fig 1.17: Schematic diagram of the jet breakup length curve [9].

1.4.1 Breaking of jet

The jet breakup process usually involves several interacting mechanisms, including the splitting up of the larger drops during the final stages of disintegration. A parameter of prime importance is the Weber number, We , which is the ratio of the disruptive aerodynamic force represented by $0.5\rho_d U_R^2$ to the consolidating surface tension force, σ/D . The higher the Weber number, the larger the deforming external pressure forces, compared with the restoring surface tension forces.

The critical condition for the drop breakup is achieved when the aerodynamic drag is just equal to the surface tension force, i.e. ,

$$C_D \left(\frac{\pi}{4} \right) D^2 0.5\rho_d U_R^2 = \pi D \sigma \quad (1.8)$$

Where C_D is the drag coefficient of the drop.

From the above equation we would get

$$We_{crit} = \frac{8}{C_D}$$

For a relative velocity U_R , the maximum stable drop size is

$$D_{max} = 12\sigma/\rho_d U_R^2 \quad (1.9)$$

If viscosity is also considered, a dimensionless number Ohnesorge is used, Oh , which is defined as

$$Oh = We^{0.5}/Re \quad (1.10)$$

Where $We = \frac{0.5\rho_d U_R^2 D}{\sigma}$ and $Re = \rho_d U_R D / \mu_d$

According to Brodkey, the effect of viscosity on the critical Weber number can be expressed as

$$We_{crit} = We_{crit} + 140h^{1.6} \quad (1.11)$$

Where We_{crit} is the critical Weber number for zero viscosity.

1.4.2 Mechanism of Jet Break up

The mechanism relies on the creation of small disturbances, either within or on the surface of a liquid jet, which promote the formation of waves that eventually lead to disintegration into ligaments and then drops. If, for any reason, this breakup time is lengthened, the breakup processes will take place further downstream, the relative velocity between air and liquid will be lower, resulting in larger drops [10-12]. An increase in liquid viscosity is one parameter that extends the breakup time. Thus, when jet break up proceeds by, an increase in fuel viscosity is always accompanied by an increase in mean drop size.

1.4.3 Theoretical Droplet size calculation

According to Rayleigh, the growth of small disturbances leads to breakup when the fastest growing disturbance attains a wavelength, λ_{opt} of 4.51d, where d is the initial jet diameter. After breakup, the cylinder of length 4.51d becomes a spherical drop so that $D = 1.89d$.

1.5 Concept and Design of micropump

In this study, a model of micro pump is designed conceptually and it is validated through CFD simulation in ANSYS Fluent, where meshes have been generated in Altair Hyper mesh. Theoretical studies have been conducted for different models of deflection in order to fix proper source of actuation for micro pump. Simulation is carried out by assuming that a periodic pressure is applied from a PZT, hence a periodic velocity boundary condition is applied at pump inlet. In perspective of implementation, a voltage supplier circuit is designed as input to PZT. Simulations have been carried out with different nozzle diameter; fluid properties like viscosity, surface tension and different actuation parameters like PZT pressure and driver frequency to optimize the pump functioning for controlled and consistent droplet discharge. Theoretical studies of other behaviour of pump like resonance and compressibility are included. Moreover thesis emphasis on characterisation of modelled micro pumps which enabled to predict the behaviour of the pump.

1.6 Literature survey

The vast majority of reported micropumps are reciprocating displacement micropumps, pumps in which moving boundaries or surfaces do pressure work on the working fluid in a periodic manner. Pistons are the moving boundaries in many macroscale reciprocating displacement pumps, but traditional, sealed piston structures have not been used in micropumps. In most reciprocating displacement micropumps, the force is applied over a moving surface which is essentially a diaphragm with fixed edges. Common pump diaphragm materials include silicon, glass, and plastic.

Figure below depicts the structure and operation of a generic diaphragm-based reciprocating displacement micropump.

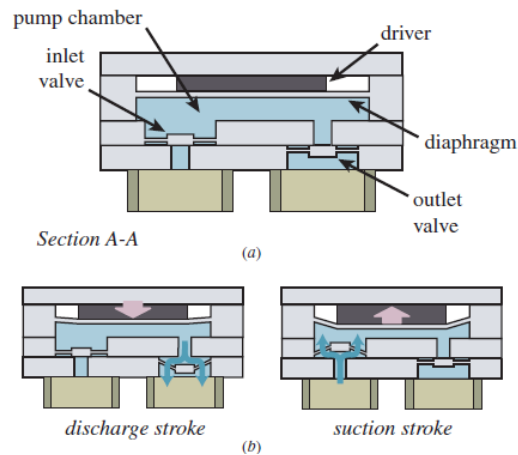


Fig1.18: Shows typical working of Piezo electric actuated micropump [2]

The basic components includes pump chamber (bounded on one side by the pump diaphragm), an actuator mechanism or driver and two passive check valves, one at the inlet (or suction side) and one at the outlet (or discharge side). The generic reciprocating displacement micropump shown in above figure is constructed from four layers of material. Micropumps made from as few as two and as many as seven layers of material have been reported. During operation, the driver acts on the pump diaphragm to alternately increase and decrease the pump chamber volume. Fluid is drawn into the pump chamber during the chamber expansion/suction stroke and forced out of the pump chamber during the contraction/discharge stroke. The check valves at the inlet and outlet are oriented to favour flow into and out of the pump chamber, respectively, rectifying the flow over a two-stroke pump cycle.

The following are some of the mechanical micropumps reported so far.

Van Lintel *et al*'s micropump comprises an entire 2 inch silicon wafer bonded between two like-sized glass plates and is therefore relatively large ($S_p \sim 4 \text{ cm}^3$). The pump chamber is a 12.5mm diameter, 130 μm deep cavity etched in the silicon wafer using an ethylene diamine/pyrocatechol/pyrazine solution (EDP) with a silicon oxide mask. Diaphragm-like check valves and connecting channels are also etched in the silicon substrate. A 0.19 mm thick glass plate seals the pump chamber side of the device; a thicker piece of glass seals the other side. The portion of the thin glass plate above the pump chamber is the pump diaphragm; a piezoelectric disk actuator is affixed to this glass diaphragm. Van Lintel *et al*'s micropump is driven by lateral strain in the piezoelectric disk. Reported performance is $Q_{max} = 8 \mu\text{l min}^{-1}$ and $P_{max} = 10 \text{ kPa}$ at $f = 1 \text{ Hz}$ and $V = 125 \text{ V}$.

Reciprocating displacement micropumps with a wide range of designs have been reported. While most micropump designs have a single pump chamber, a few micropumps have multiple pump chambers arranged either in series or in parallel as listed in the table1. Driver types and configurations vary widely; reciprocating displacement micropumps with piezoelectric, electrostatic, thermo pneumatic and pneumatic drivers among others have been reported. Various valve designs based on flaps or other moving structures have been developed, as have fixed-geometry structures that rectify flow using fluid inertial effects.

1.6.1 Modelling reciprocating displacement micropump operation.

The operation of reciprocating displacement micropumps often involves the interaction of several types of mechanics including electromechanical forces, solid mechanics and fluid mechanics. Because of this complexity, accurate, tractable, broadly applicable analytical models of reciprocating displacement micropump operation are not readily available. Low-order lumped-parameter models provide significant insight on key aspects of micropump operation [13-15]. Finite element analysis is also a useful tool in studying reciprocating displacement micropumps. [15-17]. A variety of numerical and semi analytical approaches have been taken in the study of fluid flows in reciprocating displacement micropumps[18-20] ;Studies have been performed using commercial packages to analyze the response of micropump diaphragms subjected to actuator forces [21-22].

Richter *et al* [28] and Linnemann *et al* [29] studied the relationship between compressibility ε_C and bubble tolerance by testing three micropumps very similar to one another but with different compression ratios. A micropump with $\varepsilon_C = 0.002$ was found to pump water effectively, but stalled when an 8 μl bubble entered the pump chamber. A micropump with $\varepsilon_C = 0.017$ exhibited limited bubble tolerance, stalling after two bubbles entered the chamber in succession. A micropump with $\varepsilon_C = 0.085$ consistently passed bubbles that entered the chamber.

1.6.2 Works on chamber configuration

Most reported reciprocating displacement micropumps have a single pump chamber, the micropump reported by Smits [30], however, introduced a different chamber configuration, in which the working fluid passes through three pump chambers linked in series by etched channels. Channels leading to the first and from the third chambers function as the pump's inlet and outlet. Piezoelectric actuators drive each of the three pump chamber diaphragms individually. Actuating the three piezoelectric disks 120° out of phase with one another produces net flow through the pump.

Operating in this manner, the micropump requires no valves to rectify the flow. Micropumps with multiple chambers in series and no valves operate in a manner somewhat similar to macroscale peristaltic pumps, and accordingly are sometimes referred to as peristaltic micropumps. Smits' micropump, which consists of a single etched silicon substrate sandwiched between two glass plates, was patented in the United States in 1990. It is relatively large ($S_p \sim 1.5 \text{ cm}^3$) and pumps water with $Q_{max} = 100 \mu\text{l min}^{-1}$ and $\Delta P_{max} = 600 \text{ Pa}$ operating at $f = 15 \text{ Hz}$ and $V = 100 \text{ V}_{p-p}$.

In 1990, Shoji *et al* reported [31] a micropump with two pump chambers in series. Unlike Smits' design, this micropump requires check valves. However, the two-chamber design was reported to operate effectively at higher frequencies than an otherwise-similar single-chamber micropump. Shoji *et al*'s micropump is Piezoelectric ally driven and fabricated from glass and silicon; its size is $S_p \sim 4.0 \text{ cm}^3$. $Q_{max} = 18 \mu\text{l min}^{-1}$ and $\Delta P_{max} = 10.7 \text{ kPa}$ operating at $f = 25 \text{ Hz}$ and $V = 100 \text{ V}$. Yun *et al* reported a reciprocating displacement micropump with two chambers in series driven by electro wetting-induced oscillation of a mercury plug. This micropump pumps water with $Q_{max} = 70 \mu\text{l min}^{-1}$ and $\Delta P_{max} = 700 \text{ Pa}$ operating at $f = 25 \text{ Hz}$ and $V = 2.3 \text{ V}$. P is 0.17 mW and η is 0.12%.

Berg *et al* demonstrated that pressure and flow can be generated by phased actuation of two chambers in series without use of check valves.

Shoji *et al* also reported [31] reciprocating displacement micropumps with two pump chambers arranged in parallel. This configuration was intended to reduce oscillation in the pump output due to periodic driver operation. A micropump with this parallel-chamber configuration pumps water at $Q_{max} = 42 \mu\text{l min}^{-1}$ operating at $f = 50 \text{ Hz}$ and $V = 100 \text{ V}$; ΔP_{max} was not reported. Olsson *et al* reported reciprocating displacement micropumps with two pump chambers in parallel in which drivers are attached to both the top and bottom surfaces of each pump chamber. A precision-machined brass micropump ($S_p \sim 1.6 \text{ cm}^3$) with this two-chamber, four-diaphragm design pumps water at $Q_{max} = 16 \text{ ml min}^{-1}$ and $\Delta P_{max} = 16.2 \text{ kPa}$ operating at $f = 540 \text{ Hz}$ and $V = 130 \text{ V}$. Performance improvements realized with a multi-chamber design must be balanced against increases in fabrication complexity and overall size inherent in this approach. A recent study suggests two-chamber micropump designs are particularly effective when combined with fixed-geometry valves.

1.6.3 Materials and fabrication techniques

The most common method for fabricating micropumps is micromachining of silicon combined with glass bonding layers, as seen in van Lintel *et al*'s and Smits' micropumps. These early micropumps are large by micromachining standards, each occupying an entire 2 inch silicon wafer. In 1995, Zengerle [32] *et al* reported a reciprocating displacement micropump with $S_p \sim 0.1 \text{ cm}^3$. With the pump components efficiently arranged in four layers and a compact electrostatic driver, this micropump pumps water with $Q_{max} = 850 \mu\text{l min}^{-1}$ corresponding to a self-pumping frequency, $f_{sp} \sim 1.6$. In comparison, $f_{sp} \sim 0.002$ for van Lintel *et al*'s micropump and $f_{sp} \sim 0.07$ for Smits' micropump. A number of reciprocating displacement micropumps have been fabricated through means other than traditional silicon/glass micromachining. Piezo-driven micropumps made by precision machining of brass were reported by Stemme and Stemme in 1993[33]. These micropumps are $S_p \sim 2.5 \text{ cm}^3$ in size. Two micropumps (with different valves) were reported; one pumps water with $Q_{max} = 4.4 \text{ ml min}^{-1}$ and $\Delta P_{max} = 20.6 \text{ kPa}$ operating at $f = 110 \text{ Hz}$ and $V = 20 \text{ V}$, while the other pumps water with $Q_{max} = 15.5 \text{ ml min}^{-1}$ and $\Delta P_{max} = 4.9 \text{ kPa}$ operating at $f = 310 \text{ Hz}$. The two-chamber reciprocating displacement micropump reported by Olsson *et al* was made by precision machining of brass, but with planar geometries rather than the three-dimensional geometries of the Stemme and Stemme micropumps.

Carrozza *et al* reported a micropump [34] fabricated by stereo lithography of an ultraviolet-photo curable polymer. The size of this micropump is $S_p \approx 1.3 \text{ cm}^3$; a portion of the micropump is made of brass. It pumps water with $\Delta P_{max} = 25 \text{ kPa}$ and $Q_{max} = 2.7 \text{ ml min}^{-1}$ operating at $V = 300 \text{ V}$ and $f = 70 \text{ Hz}$.

A reciprocating displacement micropump made from printed circuit boards has also been reported. The choice of pump diaphragm material can be particularly important. For micropumps driven by low frequency and/or low-force actuators, a low-modulus diaphragm material generally allows ΔV to be maximized, favourably impacting performance. Mylar and silicone rubber pump diaphragms have been used in thermo-pneumatically driven reciprocating displacement micropumps for this reason. Since the pump diaphragm comes into contact with the working fluid, however, the stability of soft polymer diaphragms is a concern.

A micropump commercially produced by Debiotech S.A. of Switzerland and targeted for implanted drug delivery has a glass diaphragm, even though it operates at $f < 1 \text{ Hz}$. This micropump produces flow rates of up to a few $\mu\text{l min}^{-1}$, suitable for therapeutic agent dispensation. For drivers capable of operating at high frequency and which produce ample force, the fast mechanical response of a stiff diaphragm generally yields the best performance. For this reason, silicon and glass are the most common diaphragm materials in piezoelectric driven reciprocating displacement micropumps. Hence in his study, silicon is considered as the material for diaphragm [35-36].

1.6.4 Drivers

Piezo electrics can be driven at frequencies over 1 kHz by electric fields on the order of 10 kV cm^{-1} or higher. The efficiency of electromechanical conversion in Piezo electrics is typically between 10 and 30% (excluding the finite efficiency of the voltage conversion and AC voltage control).

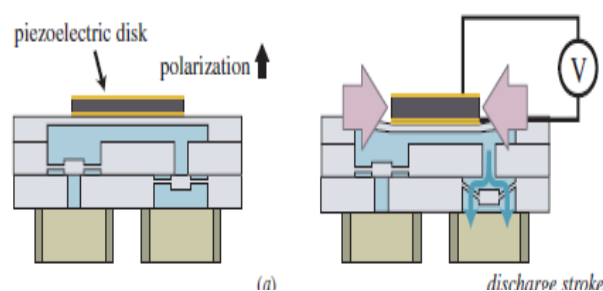


Fig 1.19: Piezoelectric transducer operation lateral

In many piezo-driven micropumps, including van Lintel *et al*'s and Smits', piezoelectric actuators are employed in a similar manner [30,36]. As shown in figure 1.19, one face of a piezoelectric disk is bonded to the chamber diaphragm (typically using epoxy); the other face of the disk is unconstrained. The piezoelectric disk is polarized in the axial direction, and each face is covered with an electrode. Applying an axial electric field across the piezoelectric disk produces both a lateral and an axial response in the disk, described by the d_{31} and d_{33} piezoelectric strain coefficients, respectively. For this configuration, the chamber diaphragm bows to balance the lateral stress in the piezoelectric disk. If the induced lateral stress in the disk is compressive, the diaphragm bows into the chamber; if tensile, it bows away from the chamber.

In some micropumps, the piezoelectric actuators are driven bidirectionally to maximize stroke volume. Progress has been made recently on the development of analytical solutions for the mechanical response of piezo bonding layer-diaphragm structures. Morris and Forster used numerical simulations to identify optimal diaphragm and piezoelectric disk geometries for lateral-strain Piezo-driven reciprocating displacement micropumps. Other researchers have also used numerical methods to study lateral strain driven reciprocating displacement micropumps. In some micropumps stroke volume is increased by using multiple electrodes to apply a spatially varying field across the piezoelectric disk. A sufficiently large number of lateral-configuration piezo-driven reciprocating displacement micropumps have been reported to permit empirical analysis of how micropump performance scales with diaphragm diameter.

1.6.5 Reported micropumps

Author and year	Driver	Valves	Construction	Chamber	Diaphragm material	Diaphragm thickness(mm)	Working fluid	f Hz
Van Lintel (1988)[36]	PZT lateral	Flap-D	Glass-Si-glass	1	Glass	0.3	water	0.1
Smits (1990)[30]	PZT lateral	None	Glass-Si-glass	3(S)	Glass	n/r	water	15
Stemme 1993[15]	PZT lateral	FG-D	Brass	1	Brass	0.2	Water Air	110
Gass (1944)[37]	PZT lateral	Flap-D	Glass-Si-glass	1	Glass	0.3	water	40
Forster (1995)[38]	PZT lateral	FG	Si-glass	1	Glass	0.15	water	114
Carrozza (1995)[34]	PZT lateral	Ball	Polymer-Brass	1	Brass	0.1	water	70
Gerlach (1995)[18]	PZT lateral	FG-ND	Si-Si-glass	1	Glass	0.12	Water Methanol	300 0
Olsson (1997)[39]	PZT lateral	FG-ND	Brass	2(P)	Glass	0.3	water	131 8
Bardell (1997)[40]	PZT lateral	FG-T	Si-glass	1	Glass	0.15	water	300
Kamper (1998)[41]	PZT lateral	Flap	Molded polycarbonate	1	Brass/Polycarbonate	0.15	water	n/r
Koch (1998)[42]	PZT lateral	Flap-C	Si-Si-Si	1	Silicon	0.07	Ethanol	200
Linnemann (1998)[43]	PZT lateral	Flap-C	Si-Si-Si	1	Silicon	0.04	water	220

Table 1. (Continued)

Author and year	Driver	Valves	Construction	Chamber	Diaphragm material	Diaphragm thickness(mm)	Working fluid	f (Hz)
Stehr (1996)[44]	PZT lateral	None	Perspex-Si	1	Silicon	0.018	water	190
Essahi (1989)[45]	PZT axial	Flap(tethered)	Si-Si	1	Silicon	0.05	water	30
Shoji 1990[46]	PZT axial	Flap(tethered)	Glass-Si-glass	1	Silicon	0.025(bossed)	Water	50
Li(2000)[47]	PZT axial	Flap-D	Si-glass (7 layers)	1	Glass	0.025	Silicon oil	3500
Zengerele (1995)[32]	Electrostatic	Flap-C	Si	1	Glass	0.15	water	300
Van de Pol (1990)[48]	TP-B	Flap-D	Glass-Si-Si-Si-Glass	1	Silicon	0.018	water	1
Tsai (2002)[49]	TP-B	FG-ND	Glass- Si	1	Glass	0.12	Isopropyl alcohol	400
Rapp (1994)[50]	Pneumatic	None	Gold-polymide	3(S)	Titanium	0.003	water	5
Bohm (1999)[51]	Electro-mag	Flap-D	Molded Plastic	1	Silicon rubber	0.2	water	264
Yun (2002)[52]	Electro-wet	Flap-C	Glass-SU8-Si-Si	2	Silicon rubber	0.08	water	n/r

Table 1.1 shows some of the mechanical micropumps reported [2]

D – Diaphragming mesa, C - Cantilever, S –Serial, P – Parallel, FG- Fixed geometry, ND – Nozzle Diffuser, n/r – not reported, T - Tesla

1.6.6 Miscellaneous works

Micropumps with various types of actuations are being used in microfluidic transport for liquid drug delivery. Due to the complexity of the flow field, particle transport through a valveless micropump might be challenging in comparison to a pressure-driven flow micropumps. Many researches have done computer simulations to find an optimum design for the delivery of drug particles through valves micropumps.

A number of micropumps for use in drug delivery has been designed, fabricated, and investigated [53-54]. Bourouinay *et al.* [55] designed and simulated an implantable medical drug-delivery system to determine the micropump dimensions and guide the fabrication. Razzackia *et al.* [56] reviewed the capabilities of existing microfabrication devices and their applications in controlled drug-delivery microsystems and concluded that the next generation of drug-delivery systems—fully integrated and self-regulating—would not only improve drug administration but also revolutionize the healthcare industry. Mailler *et al.* [57] conducted dynamic analysis for the design of a new controlled drug-delivery system with low cost high-performance silicon micropump developed for a disposable drug-delivery system. Teymoor *et al.* [58] designed and simulated a novel electrostatic micromachined pump for medical drug delivery. Their proposed structure for the micropump consists of an input port and an output port, three membranes, three active membrane valves, microchannels, and three electrostatic actuation systems. Shawgo *et al.* [59] reviewed several designs that have been microfabricated for applications including micro total analysis systems and delivery of drug solutions. These studies have proven the promise of micropumps for medical drug delivery.

Various approaches to the use of microelectromechanical systems (MEMS) for drug therapy have been developed including micropumps, microvalves, microneedles, and micro reservoirs, and these devices have shown promise *in vitro* and *in vivo*. Valveless micropumps with variable geometry and actuating mechanisms are receiving attention due to their unique properties for many biological and synthetic particle transports in drug-delivery applications. Different actuation mechanisms including electrostatic, piezoelectric, electromagnetic, pneumatic, thermo-pneumatic, magnetic, and shape memory alloys have been used in micropump designs [60]–[65]. In terms of micropump geometry, the nozzle–diffuser configuration has been successfully employed in many applications including sorting particles and cells using electrophoresis [66] and genomic analysis [67]. In order to better understand and optimize the designs, Nabavi [68] reviewed the governing steady and unsteady flows

through micropumps and microdiffusers. Eames *et al.* [69] developed an analytical model for the flow in valveless micropumps.

The development of lab-on-a-chip devices for biomedical and environmental applications requires transport of drug particles through micro devices [70]–[74]. Some examples of these devices include drug dispensing systems, deoxyribonucleic acid and protein separation chips, and blood-cell separation systems that involve microfluidic components. Ai *et al.* [75] numerically investigated particle transport through a pressure-driven mechanism in a micro channel by the arbitrary Lagrangian–Eulerian method. Their numerical analysis was carried out on a converging–diverging micro channel, and they investigated the effects of geometry, applied pressure gradient, and particle size. Koombua *et al.* [76] presented a new design concept in valveless micropumps consisting of moving walls for fluidic transport. This design concept with moving actuation membrane on side walls has been recently investigated for particle transport and delivery.

Recently, Zhang *et al.* [78] has reviewed methods for counting particles in microfluidic applications. There are very few drug-delivery micro devices in actual use today that can result in directed transport of particles and small volumes of liquid media, as the technical challenge of producing these is enormous [79]. For this reason, the investigation of the characteristics of fluid flow and particle transport in micro devices, such as, micropumps, is important and necessary for understanding drug-delivery mechanisms and improving the performance and optimizing the designs for bio- MEMS applications.

Some of the major works on micropumps are given below.

1. Design for drug delivery simulation with nozzle diffuser elements [80].

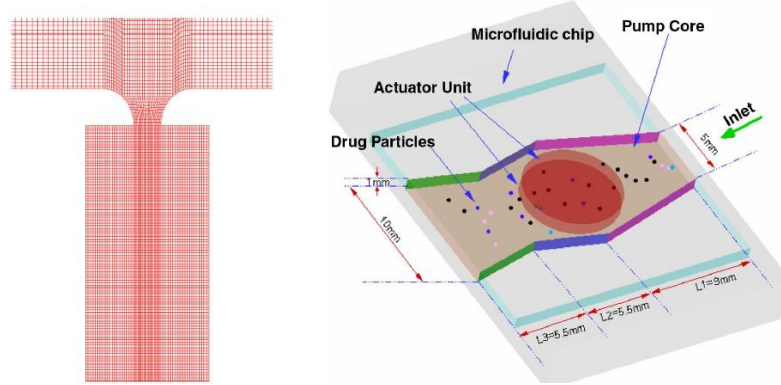


Figure. 1.20. (a) Shows DoD generator (b) Schematic diagram of MDG pump chamber and its dimensions.

The specified actuation in the micropump is achieved by a piezoelectric actuator that can be accurately controlled through an externally supplied voltage. The overall performance of the micropump is determined by specific actuation mechanism and the resulting flow through the micropump. In contrast to the existing valveless micropumps, the proposed design provides a new way for transporting liquid drug delivery using three nozzle/diffuser elements with actuating membranes.

A user-defined function written in the C programming language was used to control the movement of the actuation units mounted on top and bottom of the micropump. While the fluid-membrane interaction can affect the movement of the membrane, this effect is neglected in this paper. The actuation unit on both top and bottom walls moves in the opposite way governed by the following expression to create periodic volume expanding and contracting of the micropump chamber

$$s(r, t) = A \sin \frac{\pi r}{R} \sin 2\pi f t \quad (1.12)$$

where $s(r, t)$ is the displacement of the wall in vertical direction and f is the vibrating frequency of the micropump chamber. The expected operating mode of the micropump is that the fluid can be pumped from the inlet to the outlet.

They have compared two types of droplet generator designs i.e., DoD (droplets on demand) generator and MDG (Micropump droplet generator), where DoD generators are under the class

of current generators. Computational simulation modeling of the new MDG was developed and validated with comparisons to experimental data for current generators. Most importantly, the input power required by the newly proposed device (MDG) was several orders of magnitude below existing DoD generators for a similar droplet output.

Their study investigated the production of liquid droplet by a valveless micropump consisting of three nozzle/diffuser elements. CFD simulations combined with VOF two-phase flow modeling was performed. The results obtained illustrate the feasibility of the MDG and the relationships between actuation frequency, fluid flow, and droplet properties.

2. Optimized Design of multimaterial micropump [81].

This paper presents a micropump fabricated from low cost materials with specific goal of cost reduction. The micropump does not require any valve flap and comprises one plastic pump polyether-ether-ketone (PEEK) body, one metal diaphragm, and three piezoelectric ceramics to form piezoelectrically actuated diaphragm valves. The valve actuation simplifies micropump structural designs and assembly processes to make the pump attractive for low cost biomedical drug delivery applications.

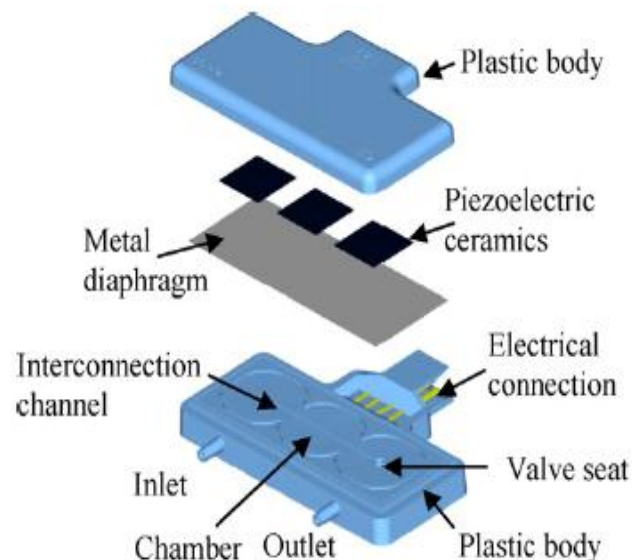


Figure 1.21: shows exploded view of proposed micropump

A detailed parameter design analysis and optimization of piezoelectric diaphragm has been performed based on 3D finite element method (FEM). An optimized geometric dimensional design: the ratio of thicknesses between the piezoelectric ceramics and the metal diaphragm, and the lateral dimension of the piezoelectric ceramics length, has been obtained and based on the optimized parameters, a micropump was fabricated and tested.

3. A novel two-stage backpressure independent micropump: modeling and Characterization [82].

A novel design of a piezoelectric silicon micropump is proposed, which provides a constant flow rate over a wide backpressure range of up to 30 kPa. This highly appreciable feature is based on a new serial arrangement of two active valves and relies on both an appropriate electrical actuation sequence of the piezo-actuators and an immanent limitation of the membrane deflection by the valve seats. The design is optimized for the low flow regime ranging from 0.1 to 50 $\mu\text{l min}^{-1}$. A detailed lumped-parameter model is derived in order to reveal the physics behind this pumping principle and to identify the optimum control scheme.

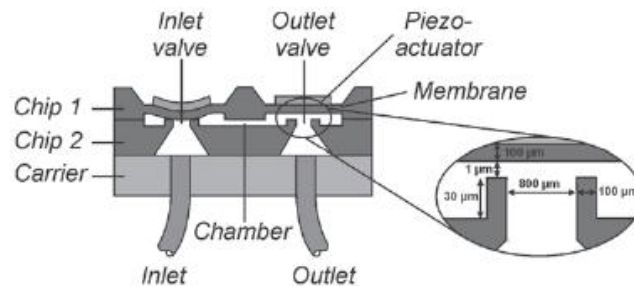


Figure 1.22: Shows schematic cross-section of the piezoelectric micropump with a close-up of the valve geometry.

This micropump provides a backpressure independent flow rate which enables true volumetric dosing. The decline of the flow rate for increasing backpressures is a severe drawback of most micropumps published so far and has bothered MEMS researchers for many years. In this design, they manage to overcome this problem by means of a proper electrical actuation scheme and an inherent stop of the membrane deflection caused by the valve seats. As a result, these features constitute a constant cut-off pressure that remains in the pump chamber after each pump cycle. An analytical model of the micropump has been set up and lumped-parameter simulations were utilized to identify suitable actuation schemes.

4 .Modeling and characterization of a nanoliter drug-delivery MEMS micropump with circular bossed membrane [83].

AMEMS micropump with circular bossed membrane designed for nanoliter drug delivery is characterized in this paper. A quasistatic model under consideration of low operating frequency is used to characterize this micropump. Characterizations of bossed membrane and microvalves are carried out separately in the finite element analysis package. The stroke volume of the membrane is calculated within the range that the linear deflection theory is valid.

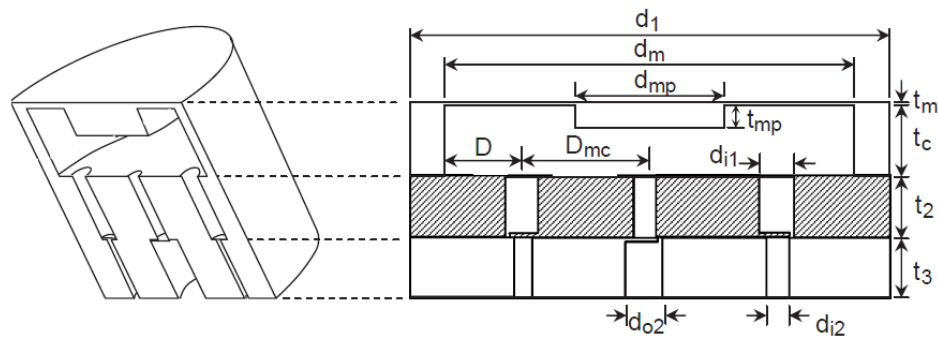


Figure 1.23: Shows critical parameters and dimensions of proposed micropump

A numerical example was demonstrated to lead the reader to solving the nonlinear ODE for characterizing the drug-delivery micropump. The linear deflection theory was considered for characterizing the circular bossed membrane based on stroke volume. The FEA package was used to simulate linear and nonlinear membrane deflections and to calculate the stroke volume as a function of net pressure. The pressure differences across the inlet and outlet microvalves were analyzed and simulated by using the sequential weak solid-fluid coupling in ANSYS/FLOTRAN.

5. Simulation of MEMS Piezoelectric Micropump for Biomedical Applications [84].

In this study, they demonstrated the usefulness of Finite Element Analysis (FEA) and simulation techniques in the design of MEMS micropumps. They focussed on a micropump driven by the piezoelectric effect, which in turn invokes the dominant resonance behaviour. The model considered in this study is a rectangular micropump with a piezoelectrically actuated diaphragm on its top and two valves on its bottom. The mechanical efficiency of the pump hinges on using resonance to generate sufficient motion of the diaphragm. Mechanical Event Simulation (MES) commercial software from ALGOR was utilized to simulate this motion, and thus provide a method for optimizing the design.

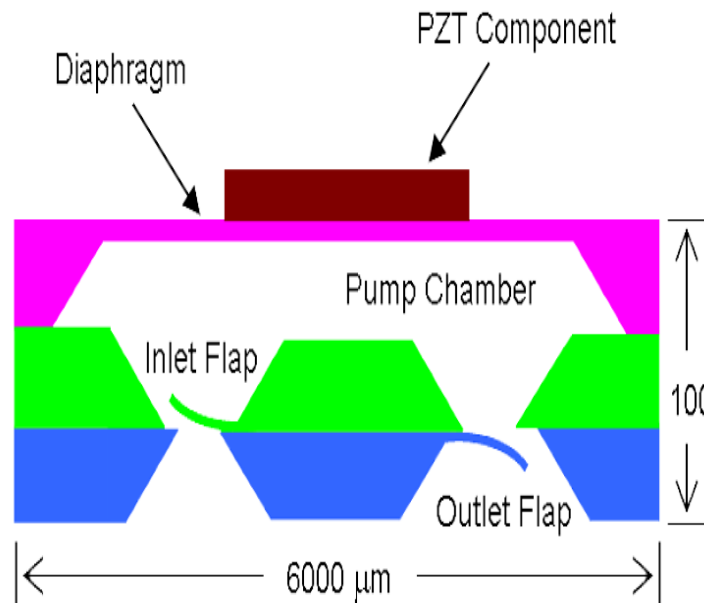


Figure 1.24 : Shows sketch of micropump cross-section. Alternating voltage causes the PZT component to expand and contract along the horizontal direction. This induces a bending stress on the diaphragm, which in turn pumps the fluid through the chamber.

1.7 Challenges and limitations

The following are the major challenges faced by the present micropumps which have been reported.

- get proper control over micropump;
- reduce response time of pump diaphragms;
- find proper actuation source for pumps;
- keep stress and strain of membrane in safe limit;
- obtain consistent and controlled droplets;
- design a pump having its magnitude of velocities in the safe range ;
- avoid air trapping inside the pump and avoid the formation of bubbles ;
- make pump flexible to use for periodic and aperiodic displacements;
- characterize the pump to its working;
- avoid high voltage required for its operation in case of PZT actuated micropumps;
- design of pumps which are reliable.

1.8 Objective

Out of the challenges mentioned above, major challenge i.e. to get consistent and controlled droplets throughout the cycles of operation was considered for the present thesis.

The main objective of this thesis is to find out a proper dimensions of the micro pump which delivers droplets of order of microliters and to find out the influence of properties of fluids, pump dimensions and actuating parameters on the droplet formation, so that optimized micro pump can be best suited for the applications in biomedical drug delivery systems, inkjet etc.

Chapter 2

Theory

Mathematical Modelling

Diaphragms are the simplest mechanical structure suitable for use as a pressure sensing element. They are used as a sensor element in both traditional and MEMS technology pressure sensors. In the case of MEMS, due to the planar nature of many established fabrication processes, the diaphragm is the main form of sensor element developed. Pressure applied to one (or both) side(s) of the diaphragm will cause it to deflect until the elastic force balances the pressure. The pressure range of a given diaphragm will depend upon its dimensions (surface area and thickness), geometry, edge conditions, and the material from which it is made.

Metal diaphragms are typically circular and may incorporate corrugations to modify diaphragm characteristics. The behaviour of a diaphragm will depend upon many factors, such as the edge conditions and the deflection range compared to diaphragm thickness. The edge conditions of a diaphragm will depend upon the method of manufacture and the geometry of the surrounding structure. It will vary between a simply supported or rigidly clamped structure, as shown in Figure 2.1. Simply supported diaphragms will not occur in practice, but the analytical results for such a structure may more accurately reflect the behaviour of a poorly clamped diaphragm than the rigidly clamped analysis. At small deflections ($< \sim 10\%$ diaphragm thickness) the pressure-deflection relationship will be linear.

As the pressure increases, the rate of deflection decreases and the pressure-deflection relationship will become nonlinear. As a rule of thumb, a deflection of 12% of diaphragm thickness will produce a terminal nonlinearity of 0.2%; a deflection of 30% produces a nonlinearity of 2%. The suitability of the deflection range will depend upon the desired specification of the micropump and the acceptable degree of compensation.

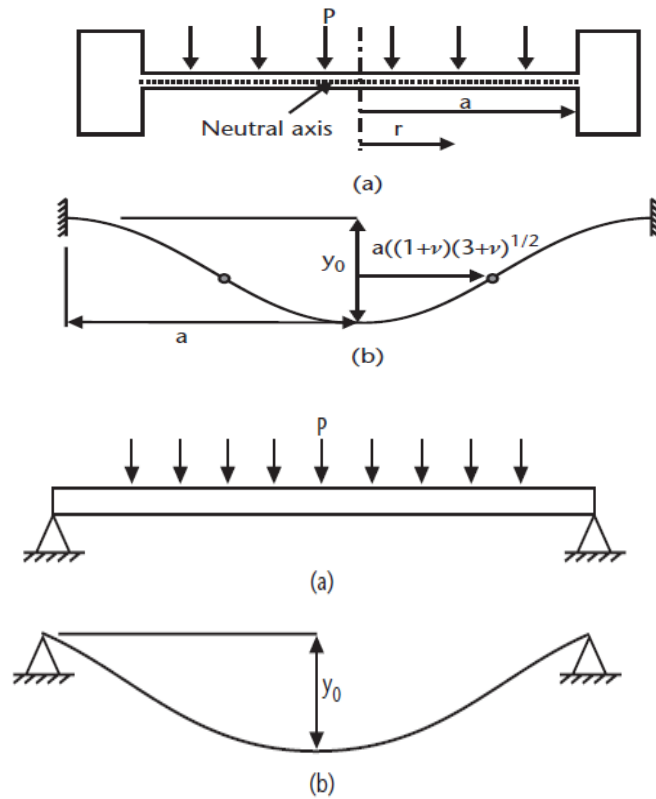


Figure 2.1: schematic of membrane deflection

The following sections present analytical equations for the deflection and of rigidly clamped diaphragms. These have been grouped according to the degree of deflection in relation to thickness, denoted as small deflection diaphragms, medium deflection diaphragms, and membranes (large deflection).

The modelling equations assume the following assumptions:

- The diaphragm is flat and of uniform thickness.
- The material is homogenous and isotropic (silicon will be covered later).
- Pressure is applied normally to the plane of the diaphragm.
- The elastic limit of the material is not exceeded.
- The thickness of the diaphragm is not too thick (e.g., maximum 20% of diaphragm diameter).
- Deformation is due to bending, the neutral axis of the diaphragm experiences no stress.

2.1 Deflection Models

There are three types of deflection models

- Small deflection model
- Medium Deflection model
- Membrane model

2.1.1 Analysis of Small Deflection Diaphragm

For small deflection diaphragms the maximum deflection is 30% of diaphragm thickness. The deflection y at radial distance r of a round diaphragm under a uniform pressure P , rigidly clamped as shown in figure, is given by

$$y = \frac{3(1 - \nu^2)P}{16Eh^3} (a^2 - r^2)^2 \quad \text{and} \quad \text{velocity} \frac{dy}{dt} = \frac{3(1 - \nu^2) (a^2 - r^2)^2}{16Eh^3} \frac{dp}{dt} \quad (2.1)$$

where h is the diaphragm thickness, E and ν are the Young's modulus and Poisson's ratio of the diaphragm material, respectively, and a is the radius of the diaphragm. The maximum deflection y_0 will occur at the diaphragm centre where $r = 0$. Assuming a common value for metals of $\nu = 0.3$, the maximum deflection is given by

$$y = \frac{0.1709Pa^4}{Eh^3} \quad (2.2)$$

Small deflection problems are typical linear problems and hence most of the non-metal diaphragms cannot be modelled as small deflection models. The stress distribution will vary both across the radius and through the thickness of the diaphragm. For example, the neutral axis (shown in fig) experiences zero stress while the maximum stress occurs at the outer faces. At any given distance r from the centre of the diaphragm, one face will experience tensile stress while the other experiences compressive stress. There are two stress components associated with a circular diaphragm: radial and tangential.

2.1.2 Analysis of medium Deflection Diaphragm

The deflection beyond 30 % of the diaphragm thickness comes under medium deflection. Both Tensile and bending stresses are considered in this case. Within the elastic limit, the characteristic equation is assumed as

$$P = \frac{16}{3(1 - \nu^2)} \frac{Eh^3}{a^4} + \frac{7 - \nu}{3(1 - \nu^2)} \frac{Eh}{a^4} y^3 \quad (2.3)$$

This may be written as the $P = cy + dy^3$

This equation consists of a linear and a non-linear component.

2.1.3 Analysis of large deflection/Membrane Analysis

Here deflection of the diaphragm is more than 500% of the thickness of the diaphragm. In theory, a membrane has no flexural rigidity and experiences tensile stress, but no bending stress. The characteristic equation for a membrane is given by

$$\frac{P(a^2 - r^2)^2}{Eh^4} = \frac{2.86y^3}{h^3} \quad (2.4)$$

Where

P - Applied pressure

a - Diaphragm radius

E - Modulus of elasticity of diaphragm material

h - Diaphragm thickness

y - Diaphragm deflection

So at Centre, $r = 0$, we get

$$\frac{Pa^4}{Eh^4} = \frac{2.86y^3}{h^3}$$

$$\text{i.e. } \frac{Pa^4}{Eh} = 2.86y^3$$

$$y = \frac{P^{0.33}(a^2 - r^2)^{2/3}}{(2.86Eh)^{0.33}} \quad (2.5)$$

The above equation is for the deflection of the diaphragm in large deflection model. So in order to obtain the velocity, the above equation is differentiated with respect to time.

Let us assume Pressure function $P = P_0 \sin^3 \omega t$, where ω - angular frequency. Here pressure function is assumed as cubic function of sine to avoid non linearity in velocity function.

$$v = \frac{dy}{dt} = \frac{P^{\frac{1}{3}}(a^2 - r^2)^{2/3}}{(2.86Eh)^{0.33}}$$

$$v(r, t) = \frac{\partial y(r, t)}{\partial t} = \frac{P_0^{\frac{1}{3}} \omega \cos(\omega t) (a^2 - r^2)^{2/3}}{(2.86Eh)^{0.33}} \quad (2.6)$$

The equation represents the velocity of the membrane at any point of time and at any point in the membrane.

2.2 Modeling the Diaphragm

Modeling diaphragm includes finding optimum radius and thickness of the same. Out of all the three models, membrane model has been preferred due to following facts.

1. It gives velocity of order of m/s to disperse droplets.
2. It accounts for the non-linearity of the diaphragm unlike in the case of small deflection model, where error would be maximum for nonlinear problems.

The following are the main constraints for modeling diaphragm.

1. Volume constraint ($a \leq 200h$) [APPX 1]

The micropump droplets volume should be of order of microliters

2. Deflection constraint ($y_0 > 5h$) [AAPX 2]

Maximum deflection of the diaphragm would be 500% more than the diaphragm thickness.

From these constraints, we can conclude that let 'a' be 200 μ m for 'h' equal to 1 μ m.

2.3 Design parameters of micropump

The analysis given below is used for reciprocating displacement micropumps operating in flow regimes characterized by both very low Reynolds number and low Reynolds number and Strouhal number product [23-25].

The pressure and flow rate generated by reciprocating displacement pumps depend on the

- (1) Stroke volume ΔV , or the difference between the maximum and minimum volumes of the pumping chamber over the course of the pump cycle;
- (2) Pump dead volume V_0 , or the minimum fluid volume contained between *the* inlet and outlet check valves at any point during the pump cycle;
- (3) Pump operating frequency, f ;
- (4) Properties of the valves;
- (5) Properties of the working fluid.

For ideal valves (ΔP forward = 0 and ΔP reverse $\rightarrow \infty$) and an incompressible working fluid, conservation of mass dictates that the flow rate is simply the product of the stroke volume ΔV and the operating frequency f . ΔV depends strongly on the characteristics of the micropump driver. Few piezo electrical drivers essentially function as displacement sources, while other drivers are well modeled as pressure sources. For displacement source-like drivers, diaphragm displacement (and therefore ΔV) is limited by the mechanical failure criteria of the diaphragm. For pressure source-like drivers, the diaphragm stiffness and dynamic response limit ΔV and f . In either case, analysis of the mechanical properties of a generic pump diaphragm is

informative. For a micropump diaphragm with diameter d_d and uniform thickness t_d clamped at its perimeter and subjected to a uniform applied driver force per unit cross-sectional area p_a , the diaphragm centreline displacement y_0 is [26].

$$\frac{p_a d_d^4}{16 E_y t_d^4} = \frac{5.33}{(1-\nu^2)} \frac{y_0}{t_d} + \frac{2.6}{(1-\nu^2)} \left(\frac{y_0}{t_d}\right)^3 \quad (2.7)$$

where E_y and ν are the Young's modulus and Poisson ratio, respectively, of the diaphragm material. The maximum stress σ in the diaphragm is given by

$$\frac{\sigma d_d^2}{4 E_y t_d^2} = \frac{4}{(1-\nu^2)} \frac{y_0}{t_d} + 1.73 \left(\frac{y_0}{t_d}\right)^2 \quad (2.8)$$

The first mechanical resonance f_r of a 'dry' diaphragm (i.e. one not subject to significant pressure forces from a liquid) is [27]

$$f_r = 2\pi (1.1015/d_d)^2 \sqrt{\frac{E_y t_d^2}{12\rho(1-\nu^2)}} \quad (2.9)$$

where ρ is the density of the diaphragm material. Equations (1) and (2), taken together, can be used to estimate the absolute upper limit on ΔV for a given diaphragm geometry, regardless of choice of driver. Equation (1) can be used to determine ΔV directly (absent an external fluid pressure differential and for quasi-static operation) for the subset of reciprocating displacement micropumps with drivers that resemble pressure sources, while equation (3) can be used to determine the range of operating frequencies for which the assumption of quasi-static response is valid.

Dynamic effects are relevant in micropumps operating at or near the diaphragm resonant frequency, potentially increasing performance but also making pump performance more dependent on valve characteristics and external conditions. ΔP_{max} for reciprocating displacement micropumps with physical drivers and valves is ultimately limited by the driver force and by the valve characteristics. In the operating regime where the driver pressure is much greater than the back pressure and the valve behaviour is nearly ideal, the compressibility κ of the working fluid limits pressure generation. For a reciprocating displacement pump with ideal valves, theoretical ΔP_{max} is [28]

$$\Delta P_{max} = \frac{1}{k} \varepsilon_C = \frac{1}{k} \left(\frac{\Delta V}{V_0} \right) \quad (2.10)$$

where the ratio between the stroke volume ΔV and the dead volume V_0 is the pump compression ratio ε_C . Because of this dependence of ΔP_{max} on ε_C , reciprocating displacement micropumps are generally capable of achieving higher pressures with liquid-phase working fluids than with gas phase. For a liquid-phase working fluid with low, uniform compressibility, ΔP_{max} is determined by the compression ratio ε_C , which is (to a degree) at the discretion of the pump designer. However, complications arise due to the very real possibility that bubbles might be present in the working fluid, increasing its compressibility and decreasing ΔP_{max} for a given ε_C . Although steps can be taken to minimize the likelihood of bubbles reaching the pump chamber, susceptibility to bubbles is a significant problem for reciprocating displacement micropumps. If bubbles are unavoidable, the compression ratio must be sufficiently large that the pump can accommodate a highly compressible working fluid.

2.4 Compressibility of Micropump

Compressibility is defined as a measure of the relative volume change of a fluid or solid as a response to a pressure change and it is given by

$$\beta = -\frac{1}{V} \frac{\Delta V}{\Delta p} \quad (2.11)$$

Where ΔV is volume change of fluid, V is the total volume, ΔP is change in pressure.

Deflection volume is determined by rotating the deflected region of $r = 0$ to $r = a$ through 360° [APPX 3].

Compressibility of the present micropump is found to be 0.01

2.5 Design of circuit for PZT

This circuit was developed to operate PZT under the voltage $V = V_0 \sin^3 \omega t$ to generate a pressure of $P = P_0 \sin^3 \omega t$. The circuit uses two sine function generator ICs with one Operational amplifier to generate cubic function of sine voltage. Here the Operational amplifier is configured as an adder. The circuit operational frequency is upto 300 kHz, where the micropump frequency is 100-250 kHz. The maximum output Voltage from the circuit is 100V which has been configured by adjusting the R_F resistors of Op Amp.

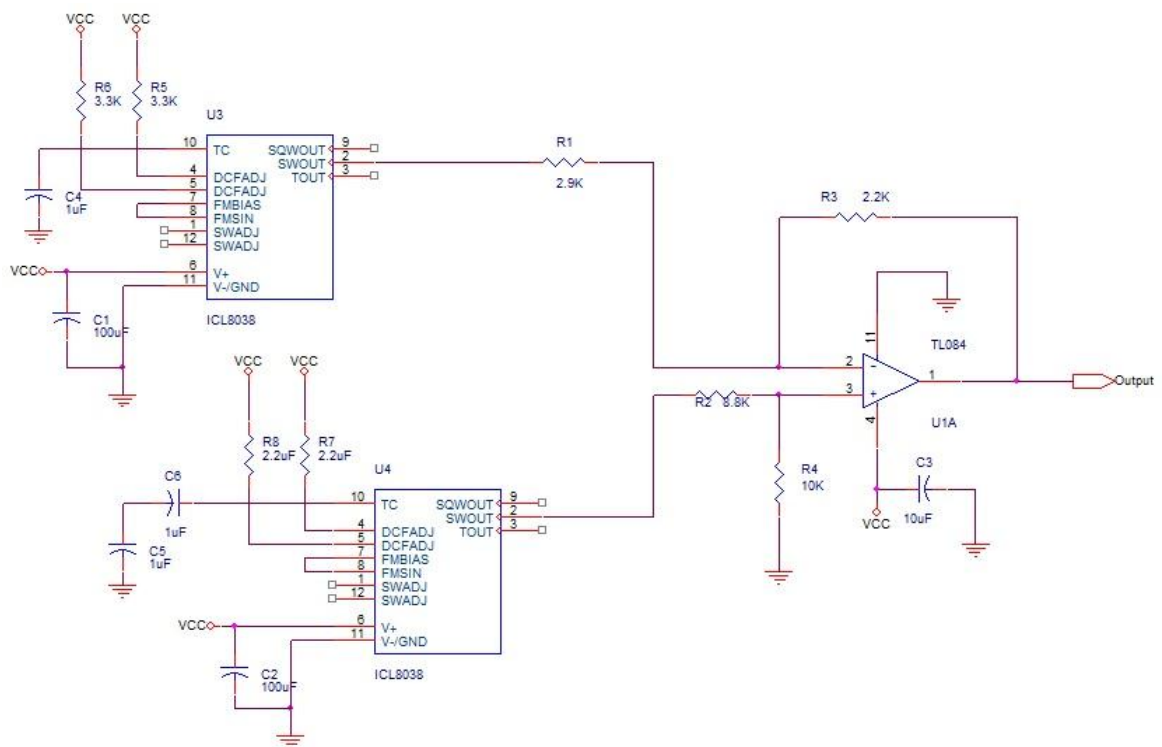


Figure 2.2: Designed voltage Supply circuit for PZT in ORCAD

Chapter 3

Numerical Procedure

The following are the procedures followed for the simulation of micropump

3.1 Meshing

3.2. Simulation

3.1 Meshing

Meshing is the first and foremost step for the simulation process. It includes finding the dimensions for the micropump and discretizing the domain into finite volume cells. Meshing has significant impact on rate of convergence, solution accuracy and CPU time.

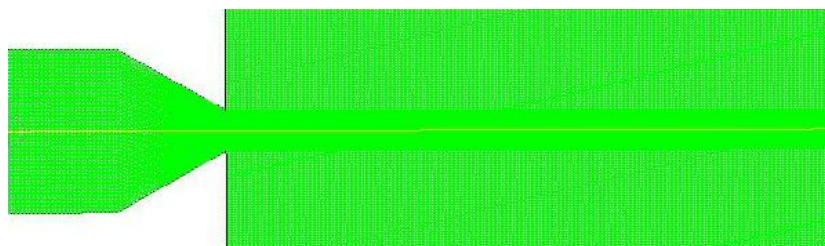


Fig 3.1: Shows the meshed domain (converged) of micropump created on Altair-Hypermesh

3.1.1 Dimensions

Region	Dimensions
Pump Inlet diameter	400μm
Nozzle diameter	100μm
Spray domain diameter	600 μm
Length of cylindrical region	250 μm
Length of conical region	250 μm

Table 3.1: Shows the dimensions of the micropump

3.1.2 Meshing Procedure

Modelling has been done with the above dimensions and used interactive meshing tool of Altair-Hypermesh, where custom meshing could be done unlike in the case of auto meshing tool. After meshing, the mesh was subjected to quality testing and following results were obtained.

Quality Parameters	Value	Fail value
Max angle quad	121	140
Min angle quad	36	40
Max angle tria	110	120
Min angle tria	29	30
Jacobian	0.6	0.98
Skew	25	40

Table 3.2: Shows the quality parameter values of the mesh (converged)

3.2 Simulation

After quality testing, the mesh is saved as Hypermesh data base format with extension “.hmascii ”. The imported mesh is applied with boundary conditions, and simulated as VOF multiphase problem. Since the mesh is symmetric with respect the axis of pump, it has been

solved as an axisymmetric 2-D problem. Simulation consists of solving the mesh with required boundary conditions and run it for certain number of time steps.

Numerical aspects of VOF model is explained as follows.

3.3 VOF MODEL

The VOF model can model two or more immiscible fluids by solving a single set of momentum equations and tracking the volume fraction of each of the fluids throughout the domain. VOF model is typically used for tracking the steady or transient liquid-gas interface. In this study, VOF model with implicit formulation is used for simulation.

3.3.2 Transient VOF Calculations

The VOF formulation in **FLUENT** is generally used to compute a transient solution. Since the shape of the droplets ejected out from the nozzle depends up on the initial level of fluid in the micropump chamber, such a problem must be solved using the time-dependent formulation.

The VOF formulation relies on the fact that two or more fluids (or phases) are not interpenetrating. For each additional phase added to your model, a variable is introduced: the volume fraction of the phase in the computational cell. In each control volume, the volume fractions of all phases sum to unity. The fields for all variables and properties are shared by the phases and represent volume-averaged values, as long as the volume fraction of each of the phases is known at each location. Thus the variables and properties in any given cell are either purely representative of one of the phases, or representative of a mixture of the phases, depending upon the volume fraction values. In other words, if the q^{th} fluid's volume fraction in the cell is denoted as α_q , then the following three conditions are possible:

- $\alpha_q = 0$: The cell is empty (of the q^{th} fluid).
- $\alpha_q = 1$: The cell is full (of the q^{th} fluid).
- $0 < \alpha_q < 1$: The cell contains the interface between the q^{th} fluid and one or more other fluids.

Based on the local value of α_q , the appropriate properties and variables will be assigned to each control volume within the domain.

3.4 Volume Fraction Equation

In this case, droplets coming out from the pumping chamber should be tracked and it is accomplished by the solution of a continuity equation for the volume fraction of one (or more) of the phases. For the q_{th} phase, this equation has the following form

$$\frac{1}{\rho_q} \left[\frac{\partial(\alpha_q \rho_q)}{\partial t} + \nabla \cdot (\alpha_q \rho_q \vec{v}_q) \right] = S_{\alpha_q} + \sum_{p=1}^n (m_{pq} - m_{qp}) \quad (3.1)$$

Where m_{qp} is the mass transfer from phase q to phase p and m_{pq} is the mass transfer from phase p to phase q . The RHS of eq(a) is zero for the present study and there is no water phase mass transfer. The volume fraction equation will not be solved for the primary phase; the primary-phase volume fraction will be computed based on the following constraint.

$$\sum_{q=1}^n \alpha_q = 1 \quad (3.2)$$

The volume fraction equation may be solved either through implicit time discretisation.

3.5 Schemes Used for Simulation

In the present study, for marching time, first order implicit scheme is used and for pressure velocity coupling, PISO scheme is preferred with skewness-neighbour coupling. A value of one is used for both skewness and neighbour correction.

For spatial discretization, Green Gauss Cell based scheme is used for gradients, Body Force weighted for pressure, First Order Upwind for momentum and Geo construct scheme is used for Volume fraction.

3.5.1 The Implicit Scheme

In this simulation implicit time marching scheme is used. For that FLUENT's standard finite-difference interpolation schemes, QUICK, First Order Upwind, and the Modified HRIC schemes, are used to obtain the face fluxes for all cells, including those near the interface.

$$\frac{\alpha_q^{n+1} \rho_q^{n+1} - \alpha_q^n \rho_q^n}{\Delta t} V + \sum_f \rho_q^{n+1} U_f^{n+1} \alpha_{q,f}^{n+1} = [S_{\alpha_q} + \sum_{p=1}^n (\dot{m}_{pq} - \dot{m}_{qp})] \quad (3.3)$$

Since this equation requires the volume fraction values at the current time step (rather than at the previous step, as for the explicit scheme), a standard scalar transport equation is solved iteratively for each of the secondary-phase volume fractions at each time step.

3.6 Material Properties

The properties appearing in the transport equations are determined by the presence of the component phases in each control volume. In present study, the phases are represented by the subscripts 1 and 2, and the volume fraction of the fluid is being tracked, the density in each cell is given by

$$\rho = \alpha_2 \rho_2 + (1 - \alpha_2) \rho_1 \quad (3.4)$$

In general, for an n-phase system, the volume-fraction-averaged density takes on the following form

$$\rho = \sum \alpha_q \rho_q \quad (3.5)$$

All other properties like viscosity, velocity etc are computed in this manner. The implicit scheme treat these cells with the same interpolation as the cells that are completely filled with one phase or the other (i.e., using the standard upwind).

3.7 Solution Methods

3.7.1 PISO (Pressure-Implicit with Splitting of Operators)

The Pressure-Implicit with Splitting of Operators (PISO) pressure-velocity coupling scheme, part of the SIMPLE family of algorithms is used for pressure velocity coupling. It is based on the higher degree of the approximate relation between the corrections for pressure and velocity. Efficiency of this calculation is improved by two additional corrections i.e. neighbour correction and skewness correction with each equal to one.

PISO can maintain a stable calculation with a larger time step and an under-relaxation factor of 1.0 for both momentum and pressure. PISO with skewness correction is used for present transient calculations which take care of high degree of mesh distortion.

Since neighbour correction is used, an under relaxation factors of 0.8 and 0.2 have been used for momentum and pressure so that they sum to one.

- **Gradient**

Gradients are used for constructing values of a scalar at the cell faces and for computing secondary diffusion terms and velocity derivatives. The gradient $\nabla\phi$ of a given variable ϕ is used to discretize the convection and diffusion terms in the flow conservation equations. In present study Green Gauss Cell Based method is used.

3.7.2 Green Gauss Cell Based method

The Green-Gauss theorem is used here to compute the gradient of the scalar ϕ at the cell centre C_0 , the following discrete form is written as

$$(\nabla\phi)_{C_0} = \frac{1}{V} \sum_f \vec{A}_f \vec{\phi}_f \quad (3.6)$$

where $\vec{\phi}_f$ is the value of ϕ at the cell face centroid, computed as shown in the sections below. The summation is over all the faces enclosing the cell.

3.7.3 Body Weighted Force

Body-force-weighted scheme is used for spatial discretization for pressure. It computes the face pressure by assuming that the normal gradient of the difference between pressure and body forces is constant. This scheme has been selected as it works well as the body forces are known a priori in the momentum equations.

3.7.4 Second order upwind Scheme

Upwind scheme of second-order accuracy is used for spatial discretization in momentum. Here quantities at cell faces are computed using a multidimensional linear reconstruction approach. In this approach, higher-order accuracy is achieved at cell faces through a Taylor series expansion of the cell-centered solution about the cell centroid. Hence when second-order unwinding is selected, the face value ϕ_f is computed using the following expression.

$$\phi_f = \phi + \nabla\phi \cdot \Delta\vec{s} \quad (3.7)$$

Where ϕ and $\nabla\phi$ are the cell-centered value and its gradient in the upstream cell, and $\Delta\vec{s}$ is the displacement vector from the upstream cell centroid to the face centroid. This formulation requires the determination of the gradient $\nabla\phi$ in each cell. This gradient is computed using the divergence theorem, which in discrete form is written as

$$\nabla\phi = \sum_f^{N_{faces}} \tilde{\phi}_f \vec{A} \quad (3.8)$$

Here the face values $\tilde{\phi}_f$ are computed by averaging ϕ from the two cells adjacent to the face. Finally, the gradient $\nabla\phi$ is limited so that no new maxima or minima are introduced.

3.7.5 The Geometric Reconstruction Scheme

In the geometric reconstruction approach, the standard interpolation schemes that are used in **FLUENT** are used to obtain the face fluxes whenever a cell is completely filled with one phase or another. When the cell is near the interface between two phases, the geometric reconstruction scheme is used.

The geometric reconstruction scheme represents the interface between fluids using a piecewise-linear approach. In **FLUENT** this scheme is the most accurate and is applicable for general unstructured meshes. The geometric reconstruction scheme is generalized for unstructured meshes from the work of Young. It assumes that the interface between two fluids has a linear slope within each cell, and uses this linear shape for calculation of the advection of fluid through the cell faces.

The first step in this reconstruction scheme is calculating the position of the linear interface relative to the centre of each partially-filled cell, based on information about the volume fraction and its derivatives in the cell. The second step is calculating the advecting amount of fluid through each face using the computed linear interface representation and information about the normal and tangential velocity distribution on the face. The third step is calculating the volume fraction in each cell using the balance of fluxes calculated during the previous step.

3.8 Momentum Equation

A single momentum equation is solved throughout the domain, and the resulting velocity field is shared among the phases. The momentum equation, shown below, is dependent on the volume fractions of all phases through the properties ρ and μ .

$$\frac{\partial(\rho\vec{v})}{\partial t} + \nabla \cdot (\rho\vec{v}\vec{v}) = -\nabla p + \nabla \cdot [\mu(\nabla\vec{v} + \nabla\vec{v}^T)] + \rho\vec{g} + \vec{F} \quad (3.9)$$

3.9 Surface Tension and Wall Adhesion

3.9.1 Surface Tension

Surface tension arises as a result of attractive forces between molecules in a fluid. At the surface, however, the net force is radially inward, and the combined effect of the radial components of force across the entire spherical surface is to make the surface contract, thereby increasing the pressure on the concave side of the surface. The surface tension is a force, acting only at the surface that is required to maintain equilibrium in such instances. It acts to balance the radially inward inter-molecular attractive force with the radially outward pressure gradient force across the surface. In regions where two fluids are separated, but one of them is not in the form of spherical bubbles, the surface tension acts to minimize free energy by decreasing the area of the interface.

The surface tension model in **FLUENT** is the continuum surface force (CSF) model proposed by Brackbill et al [87]. With this model, the addition of surface tension to the VOF calculation results in a source term in the momentum equation. It can be shown that the pressure drop across the surface (along surface tension is constant) depends upon the surface tension coefficient, σ and the surface curvature as measured by two radii in orthogonal directions, R_1 and R_2 :

$$p_2 - p_1 = \sigma\left(\frac{1}{R_1} + \frac{1}{R_2}\right) \quad (3.10)$$

where p_1 and p_2 are the pressures in the two fluids on either side of the interface.

In **FLUENT**, a formulation of the CSF model is used, where the surface curvature is computed from local gradients in the surface normal at the interface. Let \mathbf{n} be the surface normal, defined as the gradient of α_q , the volume fraction of the q_{th} phase.

$$n = \nabla \alpha_q$$

The curvature, k , is defined in terms of the divergence of the unit normal, \hat{n}

$$k = \nabla \cdot \hat{n}$$

where

$$\hat{n} = \frac{n}{|n|}$$

The surface tension can be written in terms of the pressure jump across the surface. The force at the surface can be expressed as a volume force using the divergence theorem. It is this volume force that is the source term which is added to the momentum equation. It has the following form.

$$F_{vol} = \sum_{pairs\ ij, i < j} \sigma_{ij} \frac{\alpha_i \rho_i k_j \nabla \alpha_j + \alpha_j \rho_j k_i \nabla \alpha_i}{\frac{1}{2}(\rho_i + \rho_j)} \quad (3.11)$$

This expression allows for a smooth superposition of forces near cells where more than two phases are present. For the current case where only two phases are present in a cell, then $k_i = -k_j$ and

, $\nabla \alpha_i = -\nabla \alpha_j$ and Equation simplifies to

$$F_{vol} = \sum_{pairs\ ij, i < j} \sigma_{ij} \frac{(\alpha_i \rho_i + \alpha_j \rho_j) k_i \nabla \alpha_i}{\frac{1}{2}(\rho_i + \rho_j)} \quad (3.12)$$

$$F_{vol} = \sigma_{ij} \frac{\rho k_i \nabla \alpha_i}{\frac{1}{2}(\rho_i + \rho_j)}$$

where ρ is the volume-averaged density

The above equations show that the surface tension source term for a cell is proportional to the average density in the cell.

Note that the calculation of surface tension effects on triangular and tetrahedral meshes is not as accurate as on quadrilateral and hexahedral meshes. Hence in present study, meshing has been done in quadrilaterals, where surface tension is important.

3.9.1.1 When Surface Tension Effects Are Important

The importance of surface tension effects is determined based on the value of two dimensionless quantities: the Reynolds number, Re , and the capillary number, Ca ; or the Reynolds number, Re , and the Weber number, We . For $Re \ll 1$, the quantity of interest is the capillary number:

$$Ca = \frac{\mu U}{\sigma}$$

and for $Re \gg 1$, the quantity of interest is the Weber number:

$$We = \frac{\rho L U^2}{\sigma}$$

where U is the free-stream velocity. Surface tension effects can be neglected if $Ca \gg 1$ or $We \gg 1$.

3.9.2 Wall Adhesion

An option to specify a wall adhesion angle in conjunction with the surface tension model is also available in the VOF model. The model is taken from work done by Brackbill et al. Rather than impose this boundary condition at the wall itself, the contact angle that the fluid is assumed to make with the wall is used to adjust the surface normal in cells near the wall. This so-called dynamic boundary condition results in the adjustment of the curvature of the surface near the wall.

If θ_w is the contact angle at the wall, then the surface normal at the live cell next to the wall is

$$\hat{n} = \hat{n}_w \cos\theta_w + \hat{t}_w \sin\theta_w \quad (3.13)$$

where \hat{n}_w and \hat{t}_w are the unit vectors normal and tangential to the wall, respectively. The combination of this contact angle with the normally calculated surface normal one cell away

from the wall determine the local curvature of the surface, and this curvature is used to adjust the body force term in the surface tension calculation.

The contact angle θ_w is the angle between the wall and the tangent to the interface at the wall, measured inside the phase listed in the left column under wall

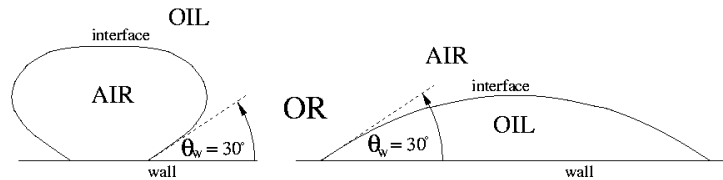


Fig 3.2: Measuring the Contact Angle

3.10 Problem Setup

In order to validate the numerical approach, simulations were performed on the mesh as shown below. The nozzle diameter is $50\mu\text{m}$. As a standard, a frequency of 250 KHz applied over the membrane, as only order of 100 kHz can give an axial velocity of order of m/s and produce droplets. No slip boundary conditions applied at the interface between fluid and the pump.

3.10.1 Initialization

Initially whole pump domain has been patched with the fluid and initiate the problem.

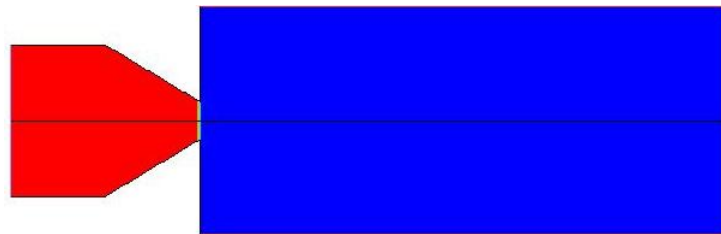


Fig 3.3: Shows initial patched domain

In the above figure red coloured patched region is the pump chamber and blue coloured is the spray domain.

As velocity vector varies and reverses on the membrane, change of pressure inside the chamber causes the fluid to expel out from the nozzle.

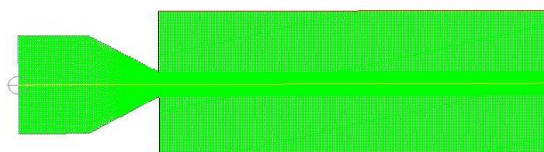


Fig 3.4: Micropump mesh

3.10.2 Grid Information

Figure shows numerical grid used for simulation of the micro pump. Quad cells have been used in meshing of micro pump. A mesh density of 26388 cells used with maximum cell squish of 0.375699 and maximum aspect ratio of 5.976. Higher grid density used in droplet path under the nozzle to capture the droplet shape variation due to hydrodynamic resistance.

3.10.3 Model Setup

Multiphase VOF model has been used for tracking the droplet from the micro pump with two Eulerian phases. Implicit scheme is used as volume fraction parameter with implicit body formulation. CFD analysis was carried out with working fluid assumed to be water with density 998.2 kg/m³ and viscosity 0.001003kg/m-s.

Two phases were defined separate for air and water as primary and secondary respectively. For water-air interaction, surface tension value of 73.5dyn/cm is used.

3.10.4 Boundary condition

Boundary conditions are defined each at the exterior partitions namely Inlet, outlet, wet wall, non-wet wall. For inlet velocity boundary conditions applied as UDF in C and volume fraction of 1 is defined at the inlet. In UDF velocity has been defined as the source from membrane which is being actuated by the PZT. For non-wetting wall a contact angle of 135 is given and for wetting wall, 90 is assigned with no slip conditions at the boundary.

3.10.5 Solution Setup

PISO scheme with skewness neighbour coupling is used as the problem is a transient one. For gradient Green gauss cell based method is used, for pressure body weighted, for momentum First order Upwind method and for Volume fraction Geo reconstruct have been used. First order implicit scheme is used for transient formulation.

3.10.6 CFD Analysis

CFD simulations analyzed the 2-D flow. The flow in the micropump is assumed to be laminar, isothermal, and incompressible. The transient laminar flow model combined with moving mesh approach was employed in order to simulate the flow field in the micropump with moving boundaries actuated by piezoelectric materials. The governing equations for the 2-D laminar flow are described by the conservation and momentum, which can be expressed as

$$\frac{\partial(\rho\vec{v})}{\partial t} + \nabla \cdot (\rho\vec{v}\vec{v}) = -\nabla p + \nabla \cdot [\mu(\nabla\vec{v} + \nabla\vec{v}^T)] + \rho\vec{g} + \vec{F}$$
$$\frac{\partial\rho}{\partial t} + \nabla \cdot (\rho \cdot \vec{v}) = 0$$

where \vec{v} is the velocity vector, p is the pressure, ρ is the fluid density, \vec{F} is the body force, and μ is its dynamic viscosity. Using the incompressible flow and assuming that the fluid density is homogenous, the mass conservation (2) becomes the divergence of flow velocity vector.. Since the homogeneous fluid flows within closed boundaries, body force due to gravity does influence the fluid motion, as the discharge of pump is vertically oriented, hence the gravitational effects on the continuous phase are considered from (1). To obtain the time dependent flow field, the above equations are solved numerically on a fluid domain with moving walls. The simulations were carried out by general-purpose computational fluid dynamics solver called FLUENT software (ANSYS/FLUENT, Inc.) with the finite volume method and the transient solution was implemented by the implicit marching techniques. A convergence criterion of 10^{-5} for residuals of mass and momentum equations was used for controlling the number of iterations. The second order accurate scheme was selected for spatial discretization to reduce the iteration error. The PISO algorithm was used for solving the pressure-velocity coupling. This procedure is repeated at every time step until a converged solution for instantaneous flow field is obtained.

3.10.7 Membrane motion

A user-defined function written in C programming language was used to control the movement of the membrane mounted on top of the micropump. Fluid membrane interaction is totally neglected in this thesis assuming its poor contribution. The membrane is being actuated by PZT and governed by the following expressions to create periodic volume expanding and contracting of the micropump chamber

$$P = P_0 \sin^3(\omega t) \quad (3.14)$$

The above expression for pressure would be the pressure input to membrane by the PZT.

$$v(r, t) = \frac{\partial y(r, t)}{\partial t} = \frac{dP^{0.33}}{dt} \frac{(a^2 - r^2)^{2/3}}{(2.86 Eh)^{0.33}} \quad (3.15)$$

The above expression would be governing expression for the membrane which is the output of the membrane and this velocity is applied to fluid mass to set its motion.

$$P = P_0 \sin^3(\omega t)$$

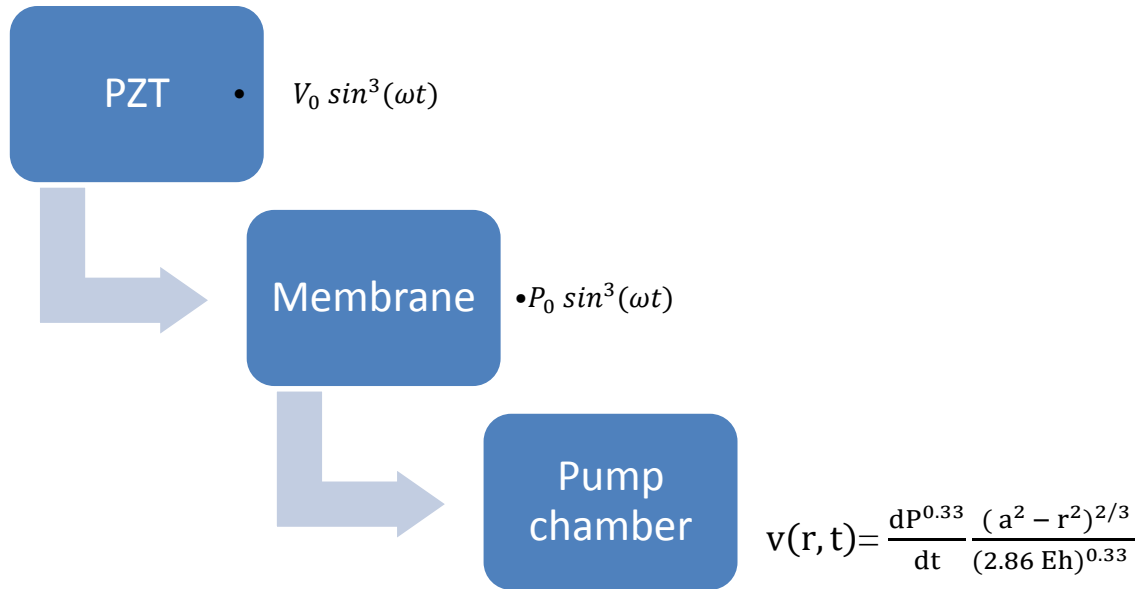


Fig 3.5: shows motion transfer from PZT to membrane

3.11 User Defined Function

To impart a velocity of above function to membrane on top of the micropump, a user defined function has been written in such a way that same velocity is imparted to the fluid over time steps. A simple UDF was written for velocity which is the inlet boundary condition for the micropump domain.

Chapter 4

Results

4.1 Grid Independency

To obtain an accurate solution, the platform at which the problem is simulated should be fine enough to get accurate values, meanwhile it should not take more computational effort.

Meshes have been created with finer grid along the droplet path in line with the nozzle and made coarser for the rest of flow domain. Initially five meshes were created named Mesh A, Mesh B, Mesh C and Mesh D in increasing order of their fineness.

Meshes created as shown below

	Mesh A	Mesh B	Mesh C	Mesh D
Cells	7300	15560	29188	65700
Grid size	x	0.75x	0.5625x	0.421x
Mesh type	Coarsest	Less coarse	Medium fine	Finest

Table 4.1: Shows meshes grid info

All the above meshes have under gone for quality test, and following reports were obtained.

Meshes	Mesh A	Mesh B	Mesh C	Mesh D
Cell squish	0.16701	0.159337	0.15699	0.151834
Aspect ratio	5.82182	5.85453	5.97069	6.02092
Nozzle cell distribution	20	60	150	450

Table 4.2: Shows meshes quality info

4.1.1 Parameters compared for grid independency

The following are the parameters which have been compared for different meshes to conduct grid independency.

- Velocity at Interface
- Pressure Variation at Inlet

Static Pressure

- Droplet velocity
- Droplet surface to volume ratio

4.1.1.1 Velocity at Interface

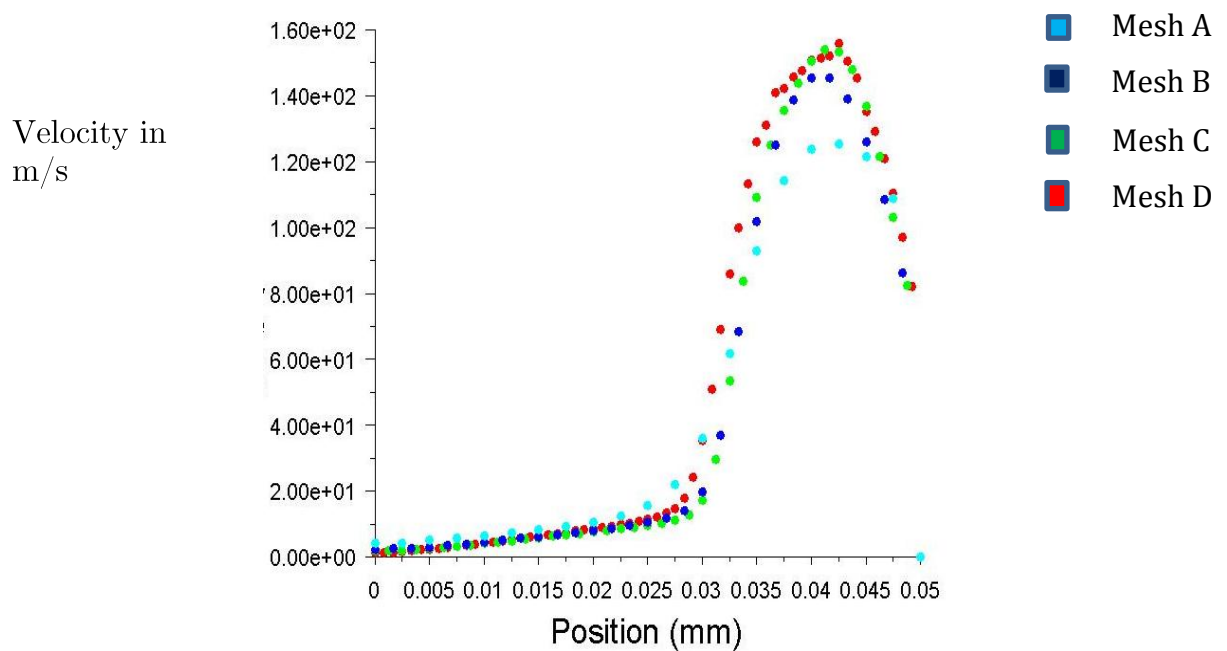


Fig 4.1: Shows plots of velocity at interface for various meshes

From the above plot it can be inferred that Mesh C almost in phase with Mesh D with less than 3% error.

4.1.1.2 Bar chart comparison for Interface Velocity

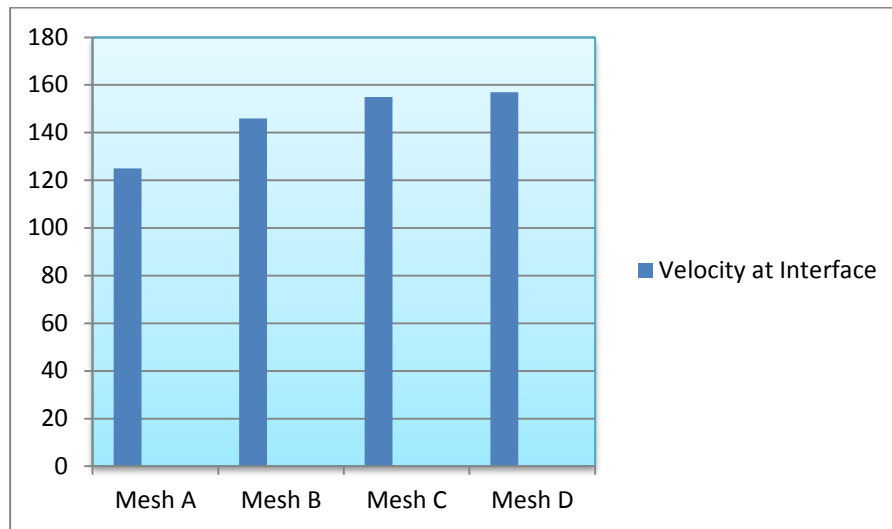


Fig 4.2: Bar chart comparison for Interface velocity

4.1.1.2 Static pressure variation at inlet

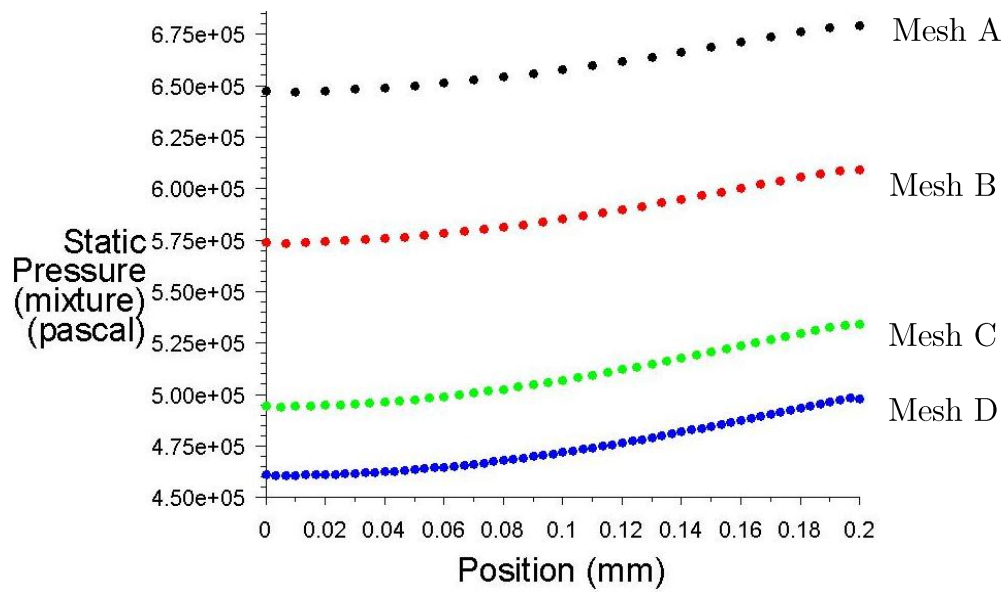


Fig 4.3: Plots of static pressure at Inlet for various meshes

4.1.1.3 Bar chart comparison for static pressure

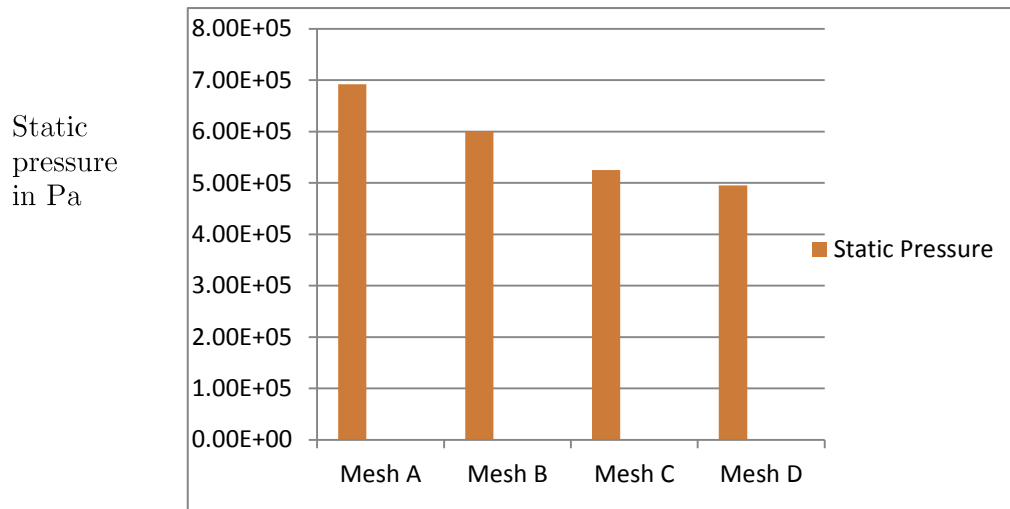


Fig 4.4: Bar chart comparison for static pressure variation at inlet

4.1.1.4 Droplet Velocity

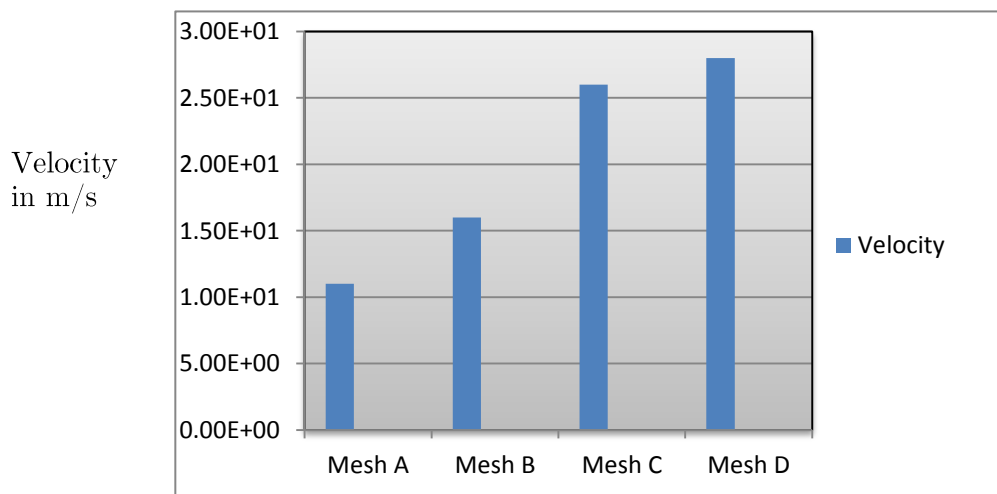


Fig 4.5 : Bar chart comparison for mass averaged droplet velocity for various meshes.

From above figures and bar charts it can be concluded that Mesh D gives more accurate result. But as from perspective of computational effort Mesh C gives value of error less than 3% of that of Mesh D. So it would be better to choose Mesh C as the final mesh for all the simulation which is the best compromised between computational effort and accuracy.

4.1.1.5 Droplet Surface to Volume ratio

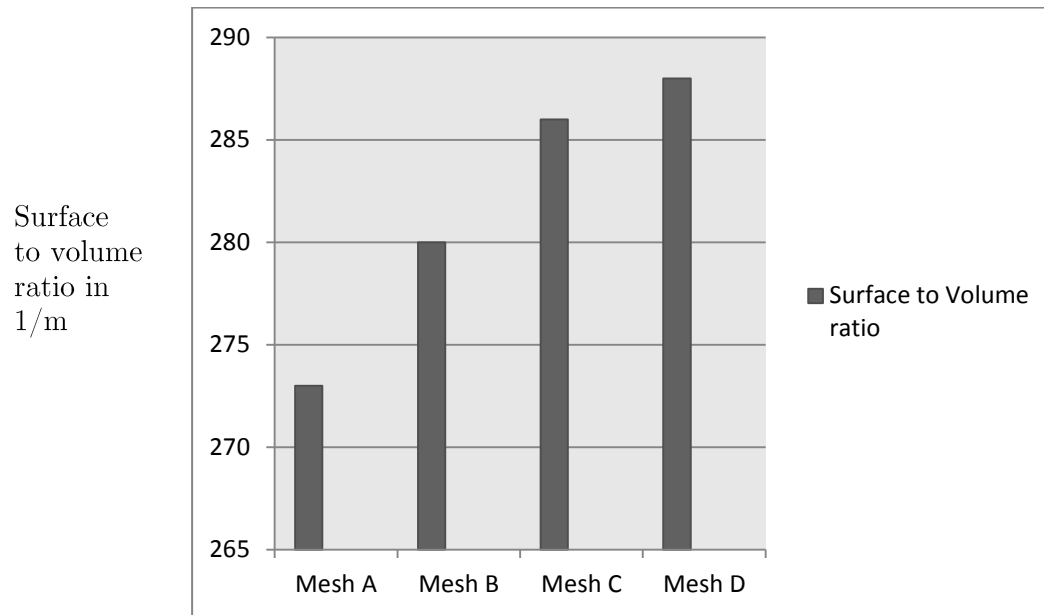


Fig 4.6: shows surface to volume ratio for different meshes at $50\mu s$

As shown in the above figure four meshes were undergone surface to volume study at $50\mu s$, as stable droplet started obtained after the same time duration. Before that surface to volume ratio would be fluctuating as shown in figure.

4.1.1.6 Fluid properties

Sl	Properties	Value
1	Viscosity(kg/m-s)	0.001003kg/m-s
2	Surface Tension(dyn/cm)	73.5dyn/cm
3	Density(kg/m ³)	998.2

Table 4.3: Shows fluid properties used in the simulation

4.2 Theory validation

4.2.1 Determination of jet regime

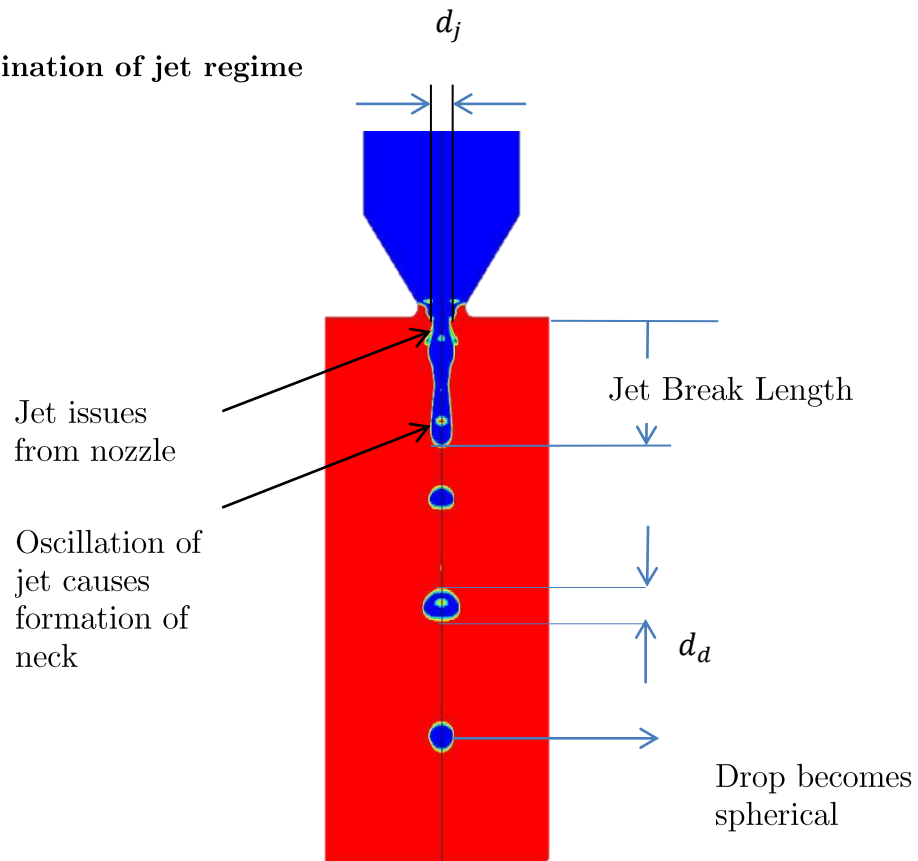


Fig 4.7: Jet break up in micropump

The above pump dispersion is under Rayleigh regime. This is proved as follows

The criteria for Rayleigh breakup is

$$We_L > 8 \quad \text{and} \quad We_g < 0.4$$

Where $We_L = \frac{\rho_L U^2 (2a)}{\sigma}$ and $We_g = \frac{\rho_g U^2 (2a)}{\sigma}$

ρ_L - Density of liquid

ρ_g - Density of surrounding gas

U - Relative velocity between jet and gas

a - Jet radius, σ - Surface Tension

The above condition corresponds to a point where the inertia force of the surrounding gas reaches about 10% of the surface tension force.

$$We_L = 998.5 \times 14.4^2 (2 \times 50.05e^{-6}) / 73.5e^{-3} = 281.69$$

$$We_g = 1.1644 \times \frac{14.4^2(2 \times 50.05e^{-6})}{73.5e^{-3}} = 0.328$$

$We_L > 8$ and $We_g < 0.4$, hence in Rayleigh regime.

But the jet breakup of the micropump is marginally in Rayleigh regime. As the velocity is fluctuating, it can be at a point of time in First wind induced regime also.

4.2.2 Determination of droplet size

Theoretical: According to Weber, the droplet size would be approximately 1.81 times the diameter of the jet

$$\begin{aligned} \text{i.e. } d_d &= 1.81d_j \\ &= 1.81 \times 50.05 \mu m \\ &= 90.5 \mu m \end{aligned}$$

Actual: Observed average diameter i.e. $d_d = 88.02 \mu m$

There is a difference of 4.5% in diameter which may be due to the following reasons

1. Weber diameter is assumed based on neglecting the real influence of gas density.
2. The nonlinear evolution after the onset of jet breakup is not considered.

$$\begin{aligned} \text{Therefore average volume of the droplet would be } V &= \frac{4}{3} \pi r^3 \\ &= \frac{4}{3} \pi (45.01e^{-6})^3 \\ &= 0.35 \text{nl} \end{aligned}$$

4.2.3 Determination of wavelength of disturbance

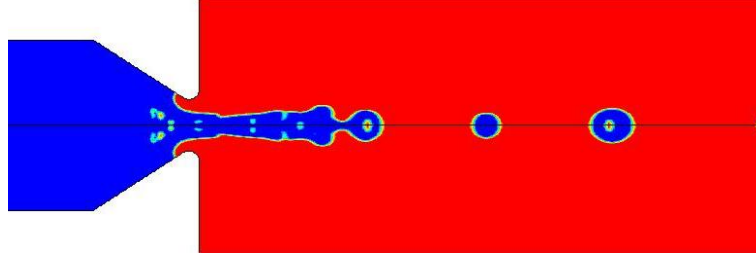


Fig 4.8: Shows the instant of a breaking of jet

Reitz generated curve-fits of numerical solutions to the dispersion equation for the maximum growth rate ω_r for the corresponding wavelength of the form $\lambda(l)$

$$\frac{l}{a} = 9.02 \frac{(1 + 0.45Z^{0.5})(1 + 0.45T^{0.7})}{(1 + 0.87We_g^{1.67})^{0.6}}$$

Where a - radius of the jet

$$Z = \frac{We_l^{0.5}}{Re_l}, T = ZWe_g^{0.5}, We_l = \frac{\rho_l U^2 a}{\sigma}, We_g = \frac{\rho_g U^2 a}{\sigma}$$

After substituting the values, we get

$$l = 447 \mu m$$

So theoretical break jet length is $447 \mu m$, while observed break jet length is $390 \mu m$. This difference might be due to many assumptions in deriving the formula for break jet length and also because of the regime we assumed. As the micropump regime marginally falls under Rayleigh regime, it could not be fully validated under this situation.

4.3 Micropump-Droplet dispersion (Base Case)

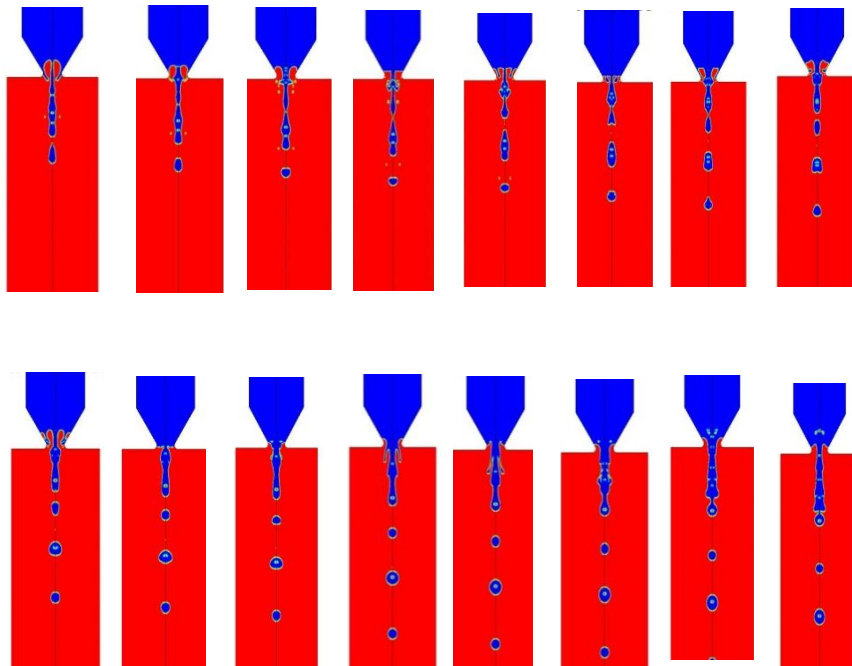


Fig 4.9: micropump working at a frequency of 250 kHz and a pressure of 60kPa from $4\mu s$ to $16\mu s$

The above base case snap shots explains the process of droplet formation in modelled micropump Droplet being dispersed from the nozzle when the external disturbing forces exceeding its surface tension. The above case is an optimized one i.e., optimized frequency, optimized pressure, optimized nozzle diameter and optimized fillet. The optimized parameters are

- 1.Frequency - 250 kHz
- 2.Pressure - 60kPa
- 3.Nozzle diameter - $100\mu m$
4. Nozzle fillet diameter - $25\mu m$

It can be noted that all these optimized values are obtained with simulation of Newtonian fluid like water. The effect of various parameters on droplet dispersion is given below.

4.3.1 Effect of frequency

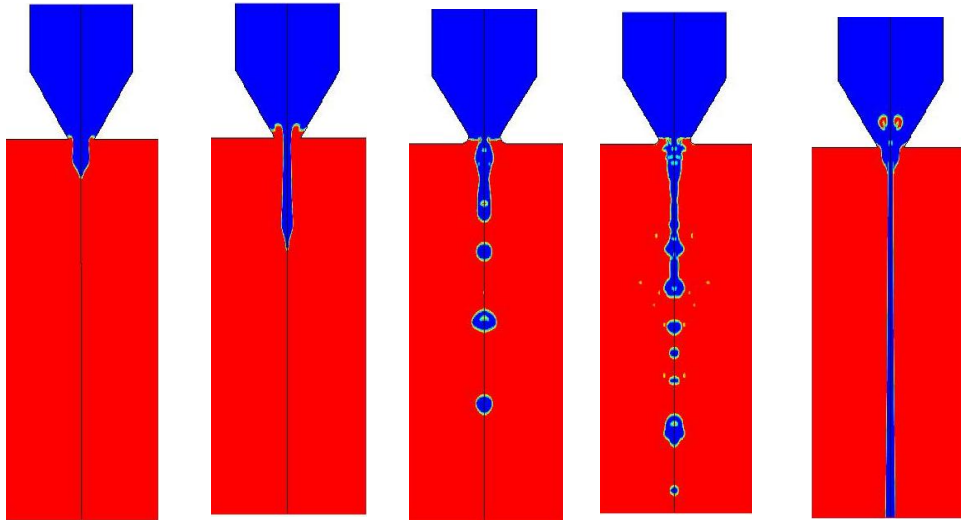


Fig 4.10 shows the instantaneous liquid droplets ejected by the micropump with different actuation frequencies at time $t = 12\mu s$

It can be observed that with the increase in actuation frequency, the droplets move faster as axial velocity of the inlet of chamber would be higher. This observation agrees with the fundamental fact that the fluid receives more kinetic energy with the faster vibration of the membrane. In addition, the higher frequency of the vibrating cycle ejects the droplets in a shorter time and more droplets can be observed at the same time interval. It can also be seen that the actuation frequency does not affect the droplets size, and the size of droplets is mainly determined by the diameter of the nozzle.

In this figure, it is observed that both the droplet velocity and volume flow rate are approximately proportional to the frequency of the micropump.

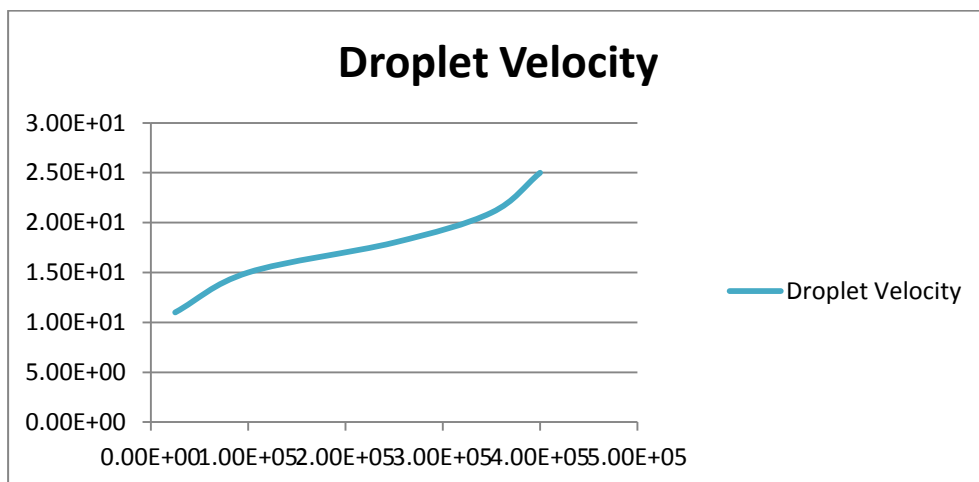


Fig 4.11: Shows Droplet Velocity Vs frequency of actuation

It is found that the droplet velocity is approximately proportional to the frequency of the micropump. In contrast, the droplet size is not affected by the frequency. The amount of droplets ejected by the micropump is determined by the frequency of actuation and thus the volume flow rate is also directly proportional to the frequency. It can be also seen that at higher frequencies instead of forming droplets, a continuous flow of liquid can be observed.

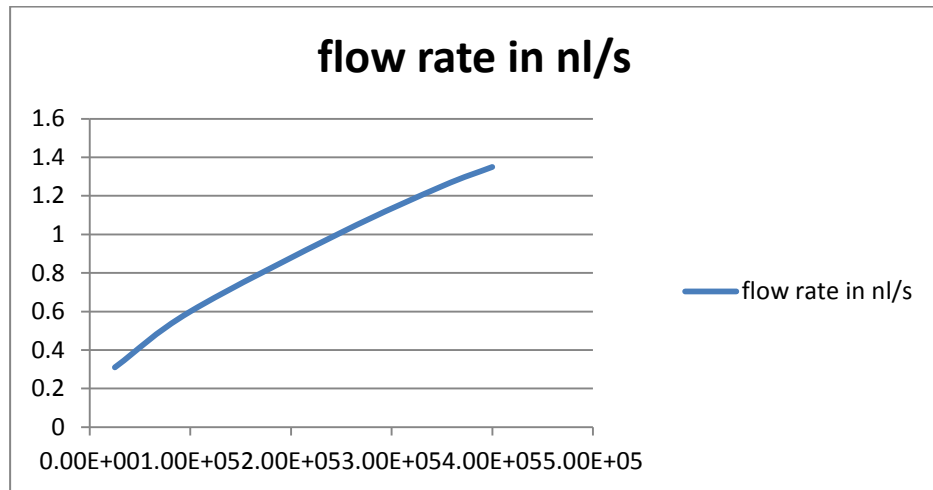


Fig 4.12: shows Plot of micropump flow rate Vs frequency

4.3.2 Effect of Nozzle diameter

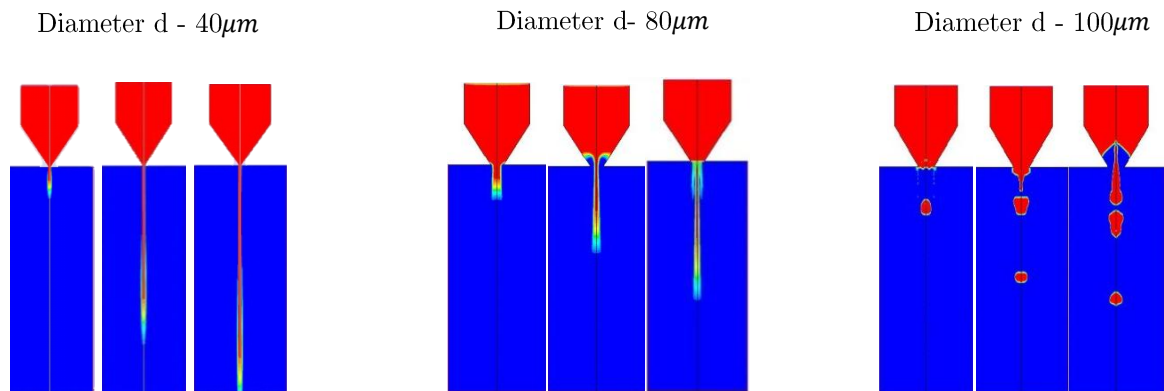


Fig 4.13: shows instantaneous liquid droplets ejected by the micropump with different nozzle diameters

To analyze the effect of the nozzle diameter on droplet generation, simulations were performed in the micropump with 250 KHz frequency with exit diameters ranging from 40 to 100µm at 32µs. It can be observed that the droplet diameter varies with the nozzle diameter. Figure below also shows that the droplets ejected by the smaller nozzle move faster than the droplets ejected by the larger nozzle diameter and continuous jet is being formed for nozzles with small diameter.

Figure 4.13 presents the effect of nozzle diameter on the droplet velocity and volumetric flow. As indicated above, the droplet velocity decreases with the increase of the nozzle diameter and the variation is not linear. Since the amount of droplets ejected out of the nozzle is determined by the actuation frequency, the average droplet velocity decreases with the nozzle diameter.

sl	Nozzle diameter(μm)	Average droplet Velocity(m/s)
1	40	92
2	80	54
3	100	23

Table 4.4: Variation of average droplet velocity with nozzle diameter

4.3.3 Effect of Pressure at $14\mu s$

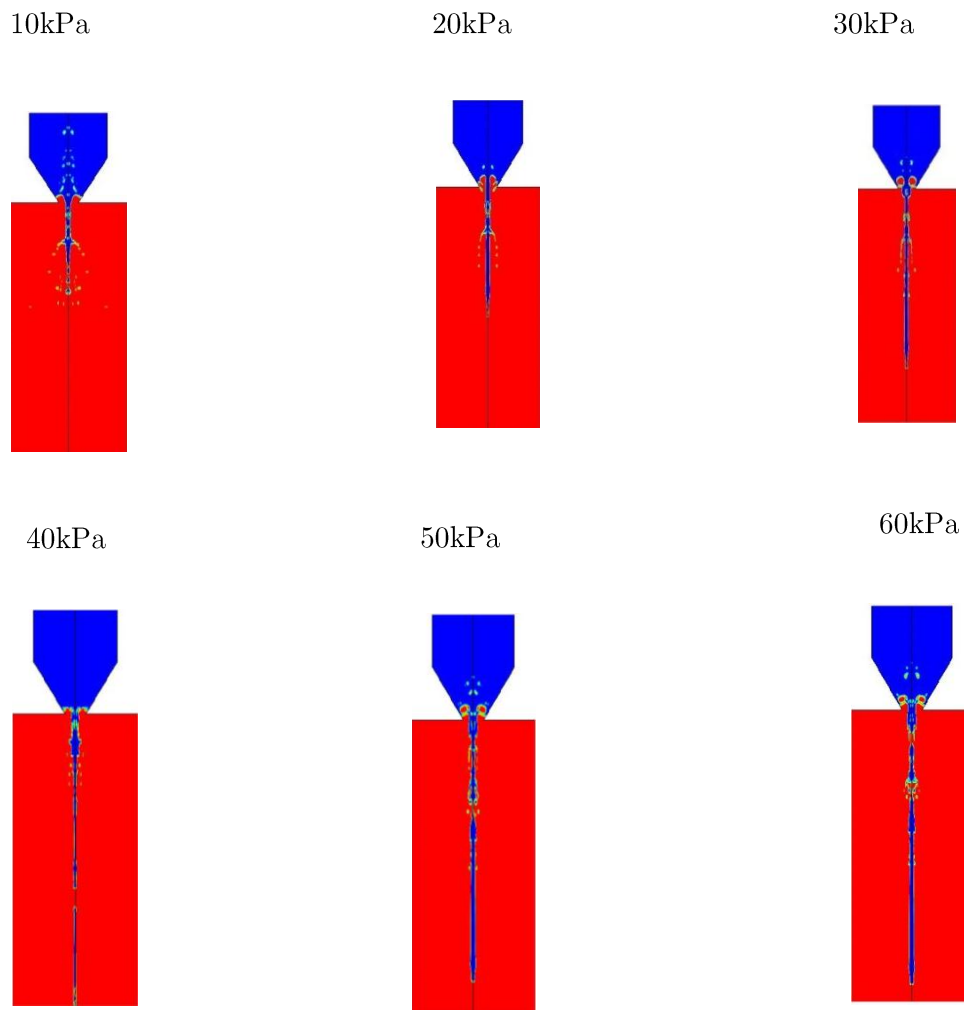


Fig 4.14: shows jet flow out of the nozzle at various pressures

From above figures, it can be inferred that as the pressure is increased more fluid is expelled out of the nozzle. From equation, it can be seen that velocity is proportional to cubic root of pressure. So droplet velocity is not that much dependent on pressure as compared to the frequency, where it is directly proportional. So pressure variations in the piezoelectric transducer are not going to affect the droplet dispersion significantly when compared to the actuation frequency.

4.3.4 Effect of liquid viscosity

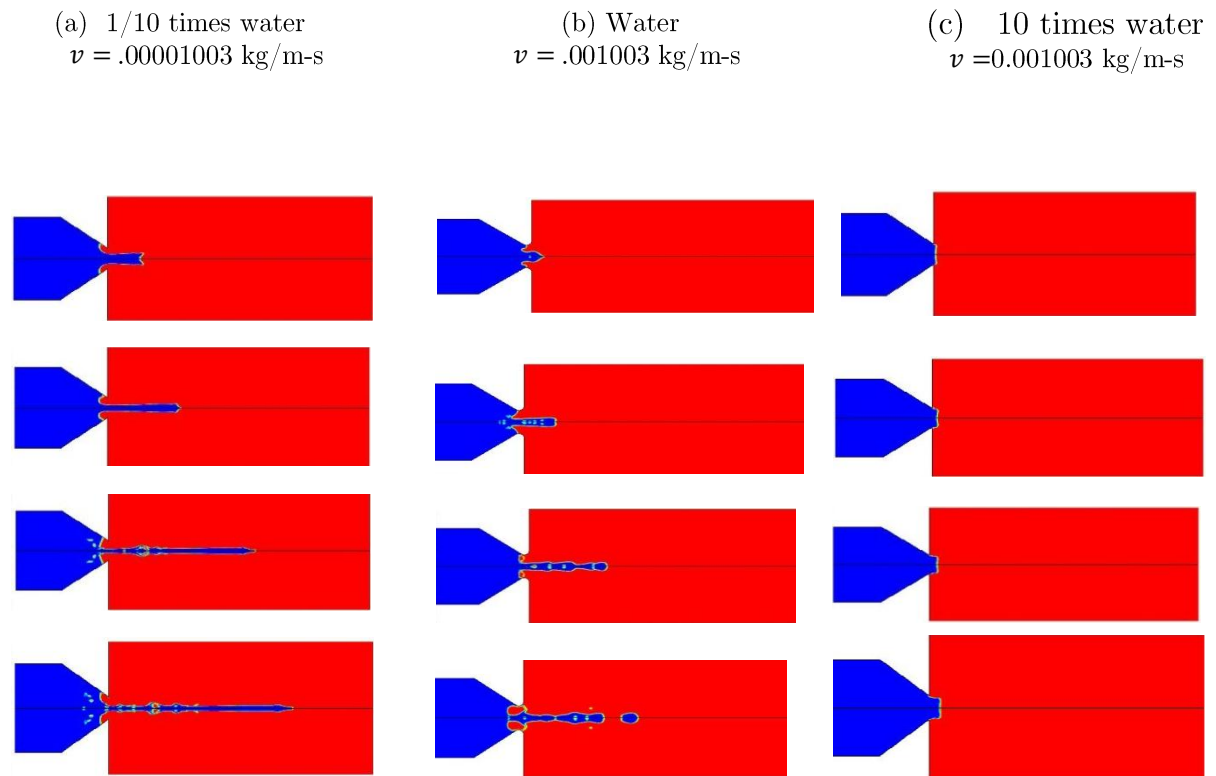


Fig 4.15: The fig shows a snapshot of droplets ejected by the micropump through the $50\mu\text{m}$ orifice at with different viscosities at 2, 4, 6, and $8\mu\text{s}$.

It can be seen that at low viscosity fluid is flowing without forming any droplets and at high viscosity droplets of large diameter tend to form because of higher cohesive force. At optimum viscosity which is equal to viscosity of water, droplets are forming due to fact that in this case, disruptive forces and surface tension is just balanced over each cycles. In the first case viscosity is less, hence surface tension would be low which causes narrow jet to fluid to flow from the nozzle which is sufficient enough to resist the aerodynamic disturbances, prevents it from forming a droplet. In the last case viscosity is too high that fluid molecules are attracted each other in another words, high cohesive force, as a result droplet of bigger diameter is being formed.

As the viscosity will modify the flow of the liquid by friction in the liquid and at the boundary, the fluid is ejected out of the micropump domain with higher velocity for the lower viscosity cases and the droplets travel faster.

4.3.5 Effect of Surface Tension

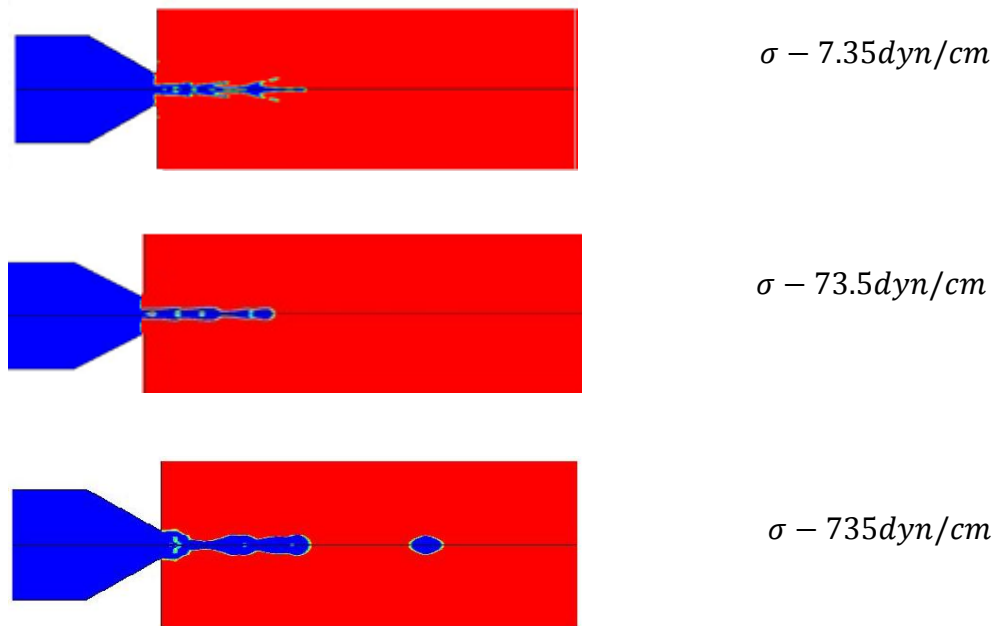
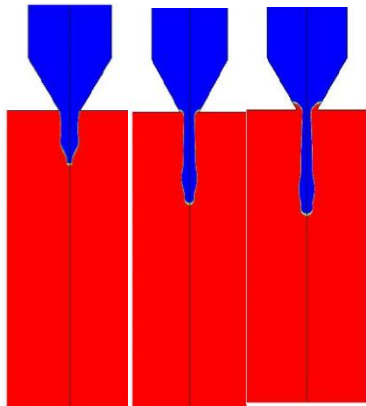


Fig 4.16: shows the effect of surface tension on the droplet size formation at time $8\mu\text{s}$

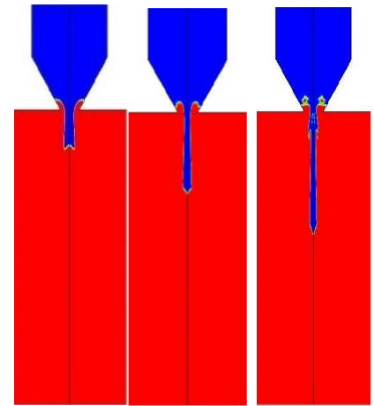
It has been observed that with the increase in surface tension, droplet size also get increased due to more cohesion of fluid molecules. Higher surface tension causes the molecules to hold together at large attractive force opposing the inertia force acting externally, hence lower the weber number. Therefore higher surface tension forces prevent fluid from forming droplets, resulting in the formation of larger droplets and smaller droplets when surface tension is lower. It has been observed that surface to volume ratio fluctuated and reaches a constant value when the droplet size is a perfect sphere.

4.3.6 Contact Angle

Hydrophobic wall

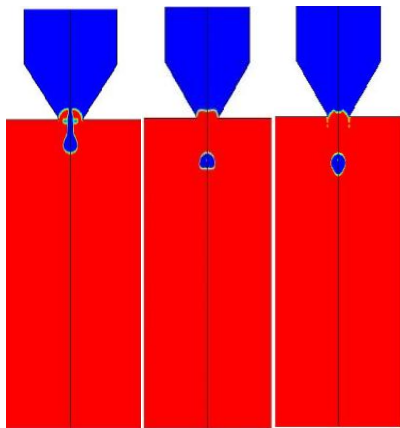


Contact angle: 165

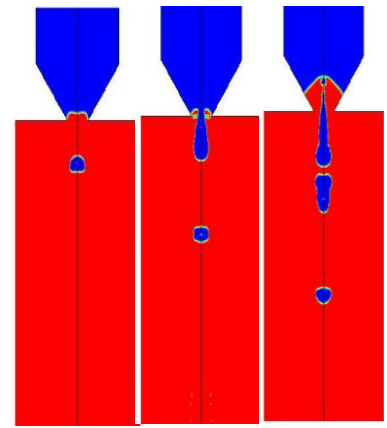


Contact angle: 135

Hydrophilic wall



Contact angle 60



Contact angle: 90

Fig 4.17: shows the droplet discharge through hydrophilic and hydrophobic pump walls over consecutive time steps

It can be seen that droplets are dispersed for hydrophilic wall only. For hydrophobic wall, we can see a continuous fluid flow instead of forming drops. The more contact angle, the more slip at the pump wall, as a result a continuous jet coming out of the nozzle. But for hydrophilic wall, velocity at the fluid at the wall is zero.

4.3.7 Effect on fillet radius

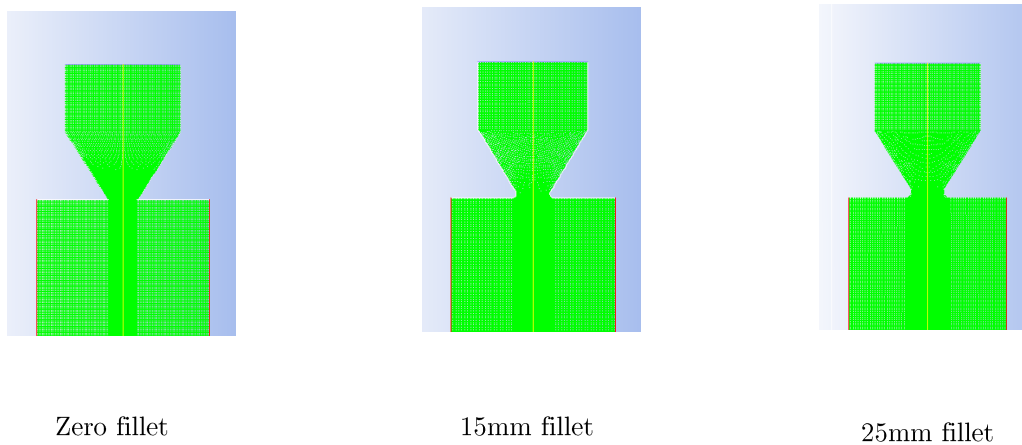
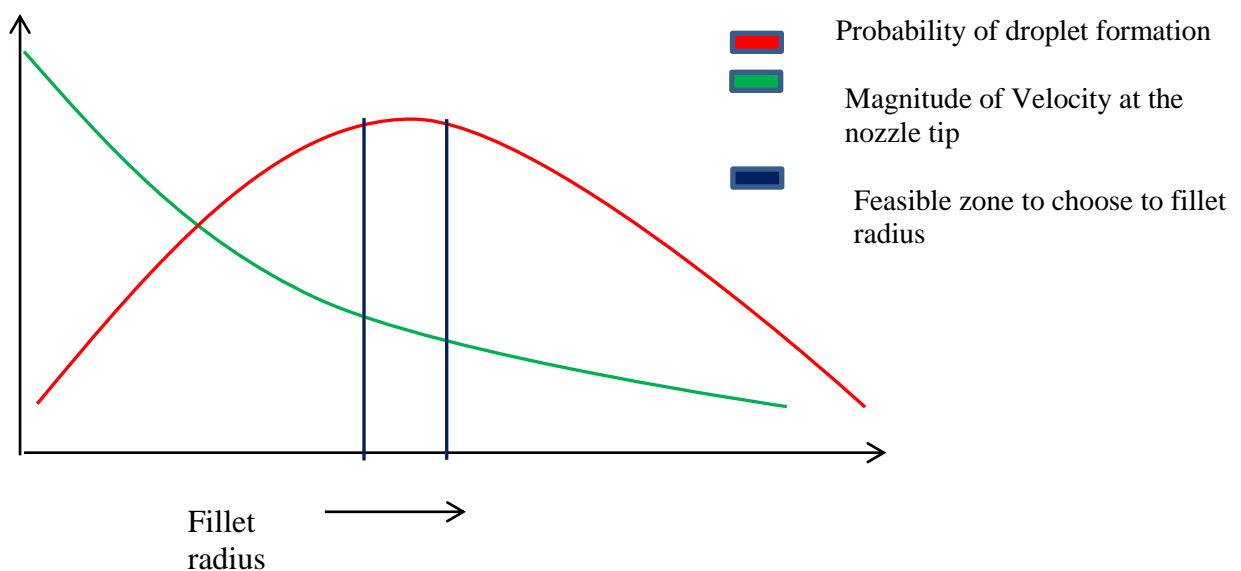


Fig 4.18: shows different meshes of nozzles with different fillet radii

Fillet is introduced to reduce the velocity at the tip of the nozzle. As sharp corner causes velocity to increase in large value, fillet radius is optimized in such a way that it compromises the magnitude of velocity and droplet formation. Higher the fillet radius, the lesser the probability of droplet formation and lower the fillet radius, higher the magnitude of the velocity at the tip of the nozzle.



4.4 Hydrodynamic resistance

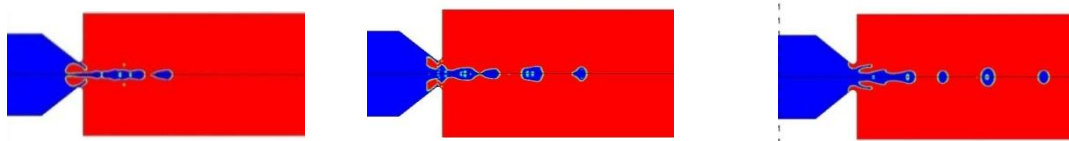
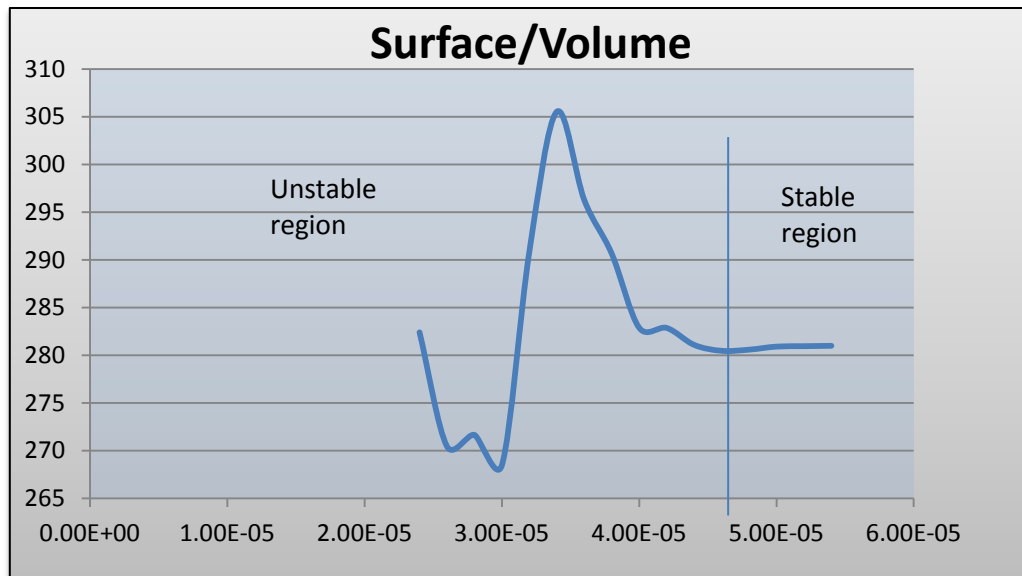


Fig 4.19 shows change in surface to Volume ratio for a droplet through spray domain

Hydrodynamic resistance is resistive force offered by the medium to the moving fluid. Due to hydrodynamic resistance, the shape and size of the droplets changes with time after they are ejected from the nozzle. Hydrodynamic resistance could be linked to droplets change in size and shape and it is responsible for the same. Rare case was selected for the study of air resistance. A droplet is tracked and its surface to volume ratio was calculated as it passes through the spraying domain.

4.5 Contours of pressure over successive cycles are given below.

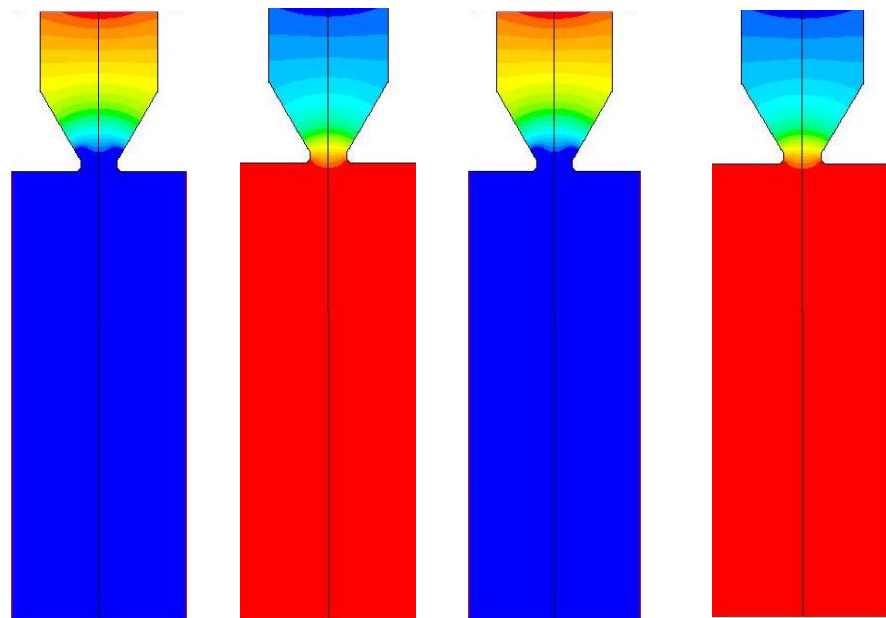
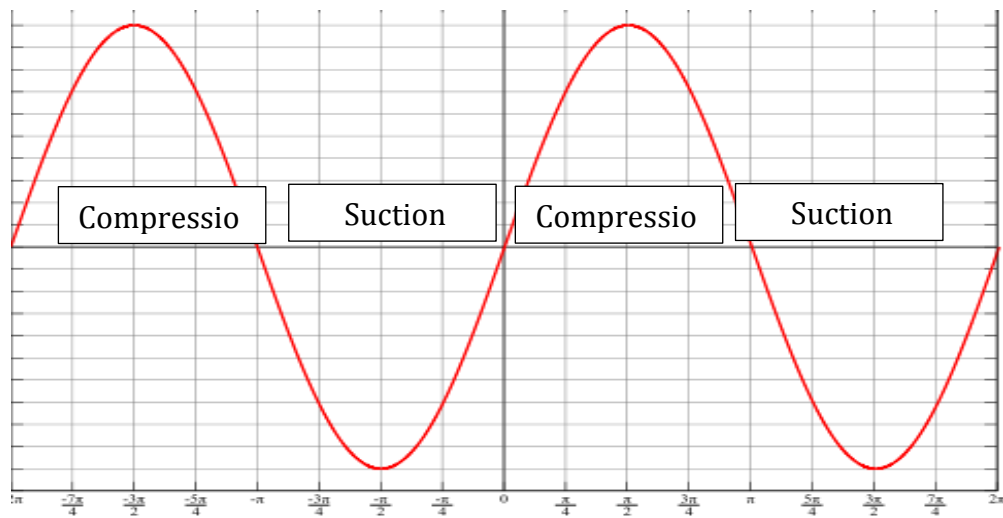


Figure 4.20 : Interior pressure contour for micropump for first two cycles of operation

Cycles	1 com	1 suc	2 com	2 suc	3 com	3 suc	4 com	4 suc
Max (MPa)	1.8	0.751	1.20	0.573	1.27	0.968	1.27	0.6
Min (kPa)	-483	-50.141	-263.94	-41.92	-3.28	-0.35	-3.63	-19.890

Table 4.5: Shows the maximum and minimum values of pressure attained over cycles

Conclusion and Scope for future work

This thesis investigated on the production of liquid droplet by a valve less micropump having a single chamber. CFD simulations combined with VOF two-phase flow modelling was performed. The results obtained illustrate the feasibility of the micropump to produce droplet under varying parameters. The primary conclusions in this study are summarized as follows:

1. It is feasible to generate liquid droplets by a valve less micropump. The droplets initially have elaborate shapes and quickly become spherical.
2. The droplet size is only affected by the outlet nozzle diameter.
3. The droplet velocity and volume flow rate are approximately proportional to the actuation frequency of the PZT.
4. The droplet velocity decreases with an increase of the nozzle diameter, as diameter decreases we can see a jet of fluid from the nozzle instead of droplet. Overall average volumetric flow rate increases with the nozzle diameter.
5. The liquid viscosity has a small influence on the droplet velocity but some effect on the volumetric flow rate and size of the droplets. As viscosity increases, droplet size increases.
6. The surface tension has strong influence on micropump, as surface tension increases the fluid particles coalesce to form a big mass of fluid.
7. Type of wall used as pump wall influences the nozzle discharge as hydrophobic wall gives continuous fluid discharge, while hydrophilic wall gives discrete discharge.

Scope for future work

The present model has been designed for the use in drug delivery systems, inkjet etc. This micropump would be a key component of the product in development aiming at the realization of a miniature pump for subcutaneous injection of insulin for diabetes care. The novelty of the system is essentially the level of miniaturization, allowing the patient to carry the pump directly taped onto the skin together with the injection soft needle. The system can be conveniently operated from a remote control device through secured RF communication. Additional benefits of the use this MEMS pumping mechanism are the improved safety, resolution, programmability and autonomy.

The model designed would be unique in the sense of actuating the membrane having a single chamber with two inlets. The nozzle is designed in such a way to obtain to get consistent droplets over period of cycles. It has been designed to run on a frequency of 250kHz. More research work can be done to run the micropump over wide range of frequencies and pressure by optimizing pump dimensions, so that controlled and consistent droplets can be obtained. The present work can be extended to non-Newtonian fluid too. Moreover consistent equi-volume droplets can be obtained by placing electric fields on the spray region opposite to each other.

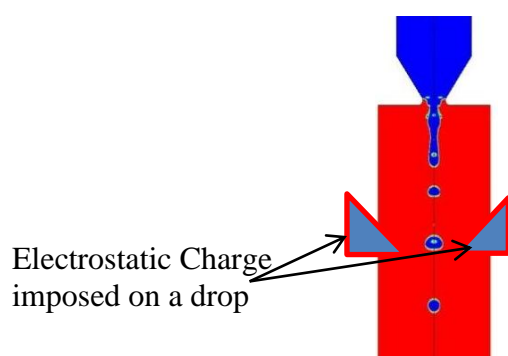


Fig 4.21: Electrostatic Charge placed in spray domain to get uniform beads [85]

To guarantee the production of uniform beads or capsules and to avoid large size distributions due to coalescence effects during the flight, the droplets pass through an electrostatic field to be charged. As a result these droplets don't hit each other during the flight and will be spread over a larger surface of the gelation bath thus resulting in mono disperse beads.

Appendix

1. Modelling the Diaphragm (Volume constraint)

We have the equation for deflection $y = \frac{P^{0.33} (a^2 - r^2)^{\frac{2}{3}}}{(2.86 Eh)^{0.33}}$

In order to obtain discharge of order of microliter, approximate deflected volume is equated to one microliter.

$$\text{i.e. } \frac{\pi a^2 h}{2} \approx 1 \mu l$$

$$\text{again } a^2 h \approx 0.636 e^{-9} m^3$$

The above constraint is the volume constraint.

2. Modelling the Diaphragm (Deflection constraint)

As large deflection has been considered here,

$$\frac{y}{h} \geq 5$$

$$\text{But we know } y = \frac{P^{0.33} (a^2 - r^2)^{\frac{2}{3}}}{(2.86 Eh)^{0.33}}$$

After substituting the values of pressure $P = 60\text{kPa}$, $E = 300\text{GPa}$, $r = 0$;

$$\text{We get } a \geq 200h$$

The above constraint is known as deflection constraint

Diaphragm dimensions are assumed based on above constraints.

Assuming a diaphragm thickness of $1\mu m$, so $a \geq 200 \mu m$

3. Compressibility of micropump

We have the equation for deflection $y = \frac{p^{0.33} (a^2 - r^2)^{\frac{2}{3}}}{(2.86 Eh)^{0.33}}$

Substituting all the values, we get

$$y = 0.4118 (4e^{-8} - r^2)^{2/3}$$

But Area = $\iint dr dx$

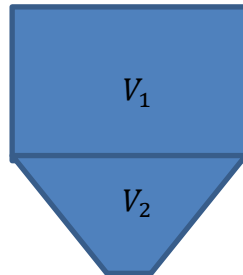
So area becomes

$$\begin{aligned} \text{Area} &= \iint_0^{0.4118 (4e^{-8} - r^2)^{2/3}} dr dx \\ &= 9.62 e^{-10} m^2 \end{aligned}$$

Volume is obtained by rotating the area 360° about the centre of axis

So volume ΔV is $4.73 e^{-13} m^3$

To find V (micropump chamber Volume)



From above figure $V = V_1 + V_2$

$$\begin{aligned} V_1 &= \pi r^2 h \\ &= \pi \times (200e^{-6})^2 \times 250e^{-6} \\ V_1 &= 3.14e^{-11} m^3 \end{aligned}$$

To find V_2

$$V_2 = \frac{h}{3} [A_1 + A_2 + \sqrt{A_1 A_2}]$$

$$\begin{aligned} A_1 &= \pi r_1^2 \\ &= \pi \times (200e - 6)^2 \end{aligned}$$

$$A_2 = \pi r_2^2$$

$$= \pi \times (25e - 6)^2$$

$$V_2 = \frac{250e-6}{3} [\pi \times (200e^{-6})^2 + \pi \times (25e - 6)^2 + \sqrt{\pi(200e^{-6})^2} \sqrt{\pi(25e - 6)^2}]$$

$$= 1.1944e^{-11} m^3$$

$$V = V_1 + V_2$$

$$= 3.14e^{-11} m^3 + 1.1944e^{-11} m^3$$

$$= 4.33e^{-11} m^3$$

$$\varepsilon_c = \frac{\Delta V}{V_0} = \frac{4.73e^{-13}}{4.33e^{-11}} = 0.01092$$

For water, the compressibility is $4e^{-10}$

$$\text{i.e. } -\frac{1}{V} \frac{\Delta V}{\Delta p} = 4e^{-10}$$

$$\Delta p = 14e^5$$

$$\Delta V_{\text{water}} = 2.4e^{-14} m^3$$

$$\text{And } \Delta V_{\text{micropump}} = 4.61e^{-13} m^3$$

So theoretical droplet volume would be equal to

$$\Delta V_{\text{micropump}} - \Delta V_{\text{water}} = 4.37e^{-13} m^3$$

$$= 0.461 \text{ nl/cycle}$$

Chapter

References

- [1] TOPICAL REVIEW A review of micropumps, D J Laser and J G Santiago
Department of Mechanical Engineering, Stanford University, Stanford, CA 94305,
USA.P Woias, Micropumps—past, progress and future prospects, S&A:B, Vol. 105,
2005, pp. 28–38.
- [2] Mechanical micropumps, Pasi kallio, Department of Automation science and
Engineering, Tampere University of Technology.
- [3] Current Micropump Technologies and their biomedical applications, Farid Amirouche,
Yu Zhou , Tom Johnson, *Microsyst Technol* (2009) 15:647–666.
- [4] Method for control of the volume flux of a liquid in an osmotic micropump and osmotic
micropump ,Ehwald R, Woehlecke H, Adleff H, Ehwald M (2006). Google Patents,
USA.
- [5] Zeta Potential in Colloid Science ,Hunter R J 1981 (San Diego, CA: Academic).
- [7] Physical Chemistry of Surfaces, Adamson A W and Gast A P 1997 (New York:Wiley)
- [8] Theoretical and experimental study of MHD ,Jang J S and Lee S S 2000
(magneto hydrodynamic) micropump *Sensors Actuators A* **80** 84–9.
- [9] Drop and spray formation from a liquid jet, S. P. Lin, Mechanical and Aeronautical
Engineering Department, Clarkson University, Potsdam, New York 13699,R. D. Reitz
Mechanical Engineering Department, University of Wisconsin, Madison, Wisconsin,
53706
- [10] Asymmetric instability of a viscid capillary jet in an inviscid media. Avital E. 1995
Phys.Fluids. 7:1162–64 Benjamin TB. 1959.
- [11] Shearing flow over a wavy boundary. *J. Fluid Mech.* 6:161–205 Bers A. 1983.
Space- time evolution of plasma instabilities absolute and convective.
- [12] In *Handbook of Plasma Physics*, ed. M. Rosenbluth, 1:452–516 Amsterdam: North
Holland.

- [13] Morris C J and Forster F K 2003 Low-order modeling of resonance for fixed-valve micropumps based on first principles *J. Microelectromech. Syst.* **12** 325–34
- [14] Bourouina T and Grandchamp J P 1996 Modeling micropumps with electrical equivalent network *J. Micromech. Microeng.* **6** 398–404
- [15] Olsson A, Stemme G and Stemme E 1999 A numerical design study of the valveless diffuser pump using a lumped-mass model *J. Micromech. Microeng.* **9** 34–44.
- [16] Moussa W A and Gonzalez U F 2002 Simulation of MEMS piezoelectric micropump for biomedical applications *Proc. ASME Int. Mechanical Engineering Congress and Exposition (New Orleans, LA)*
- [17] Morris C J and Forster F K 2000 Optimization of a circular piezoelectric bimorph for a micropump driver *J. Micromech. Microeng.* **10** 459–65
- [18] Gerlach T 1998 Microdiffusers as dynamic passive valves for micropump applications *Sensors Actuators A* **69** 181–91
- [19] Ullman A and Fono I 2002 The piezoelectric valve-less pump—improved dynamic model *J. Microelectromech.Syst.* **11** 655–64
- [20] Pan L S, Ng T Y, Wu X H and Lee H P 2003 Analysis of valveless micropumps with inertial effects *J. Micromech. Microeng.* **13** 390–9.
- [21] Gamboa A R, Morris C J and Forster F 2003 Optimized fixed-geometry valves for laminar flow micropumps *Proc. ASME Int. Mechanical Engineering Congress and Exposition (Washington, DC)*.
- [22] Koch M, Evans A G R and Brunnschweiler A 1998 The dynamic micropump driven with a screen printed PZT actuator *J. Micromech. Microeng.* **8** 119–22.
- [23] Deen W M 1998 *Analysis of Transport Phenomena* (New York: Oxford University Press).
- [24] Probstein R F 1994 *Physicochemical Hydrodynamics* (New York: Wiley).
- [25] Kundu P K and Cohen I M 2002 *Fluid Mechanics* (New York: Academic).
- [26] Young W C and Budynas R C 2002 *Roark's Formulas for Stress and Strain* 7th edn (New York: McGraw-Hill).
- [27] Geradin M and Rixen D 1997 *Mechanical Vibrations: Theory and Applications to Structural Dynamics* 2nd edn (Chichester, NY: Wiley).
- [28] Richter M, Linnemann R and Woias P 1998 Robust design of gas and liquid micropumps *Sensors Actuators A* **68** 480–6.
- [29] Linnemann R, Woias P, Senfft C-D and Ditterich J A 1998 A self-priming and bubble-tolerant piezoelectric silicon micropump for liquids and gases 11th Annual Int.

- Workshop on Micro Electro Mechanical Systems (Heidelberg, Germany) (Piscataway, NJ: IEEE).
- [30] Smits J G 1990 Piezoelectric micropump with 3 valves working peristaltically Sensors Actuators A **21** 203–6.
- [31] Shoji S, Nakagawa S and Esashi M 1990 Micropump and sample-injector for integrated chemical analyzing systems Sensors Actuators A **21** 189–92.
- [32] Zengerle R, Ulrich J, Kluge S, Richter M and Richter A 1995 A bidirectional silicon micropump Sensors Actuators A **50** 81–6.
- [33] Stemme E and Stemme G 1993 A valveless diffuser/nozzle-based fluid pump Sensors Actuators A **39** 159–67.
- [34] Gozza M C, Croce N, Magnani B and Dario P 1995 A piezoelectric-driven stereolithography-fabricated micropump J. Micromech. Microeng. **5** 177–9.
- [35] MIP Implantable product information, www.debiotech.sa
- [36] Maillefer D, van Lintel H T G, Rey-Mermet G and Hirschi R 1999 A high-performance silicon micropump for an implantable drug delivery system 12th IEEE Int. Conf. on Micro Electro Mechanical Systems (Orlando, FL) (Piscataway, NJ: IEEE).
- [37] Gass V, Vanderschoot B H, Jeanneret S and Derooij N F 1994 Integrated flow-regulated silicon micropump Sensors Actuators A **43** 335–8.
- [38] Forster F, Bardell R, Afromowitz M, Sharma N and Blanchard A 1995 Design, fabrication and testing of fixed-valve micropumps Proc. ASME Int. Mechanical Engineering Congress and Exposition (San Francisco, CA) (New York: ASME).
- [39] Olsson A, Enoksson P, Stemme G and Stemme E 1996 A valve-less planar pump isotropically etched in silicon J. Micromech. Microeng. **6** 87–91.
- [40] Bardell R, Sharma N, Forster F, Afromowitz M and Penney R J 1997 Designing high-performance micro-pumps based on no-moving-parts valves Proc. 1997 ASME Int. Mechanical Engineering Congress and Exposition (Dallas, TX).
- [41] Kamper K-P, Dopfer J, Ehrfeld W and Oberbeck S 1998 A self-filling low-cost membrane micropump Proc. 11th Annual Int. Workshop on Micro Electro Mechanical Systems (Heidelberg, Germany) (Piscataway, NJ: IEEE).
- [42] Koch M, Harris N, Evans A G R, White N M and Brunnschweiler A 1998 A novel micromachined pump based on thick-film piezoelectric actuation Sensors Actuators A **70** 98–103.
- [43] Linnemann R, Woias P, Senfft C-D and Ditterich J A 1998 A self-priming and bubble-tolerant piezoelectric silicon micropump for liquids and gases 11th Annual Int.

Workshop on Micro Electro Mechanical Systems (Heidelberg, Germany) (Piscataway, NJ: IEEE).

- [44] Stehr M, Messner S, Sandmaier H and Zengerle R 1996 The VAMP: a new device for handling liquids or gases *Sensors Actuators A* **57** 153–7.
- [45] Esashi M, Shoji S and Nakano A 1989 Normally closed microvalve and micropump fabricated on a silicon-wafer *Sensors Actuators* **20** 163–9.
- [46] Shoji S, Nakagawa S and Esashi M 1990 Micropump and sample-injector for integrated chemical analyzing systems *Sensors Actuators A* **21** 189–92.
- [47] Li H Q et al 2000 A high frequency high flow rate piezoelectrically driven MEMS micropump *Proc. 2000 Solid-State Sensor and Actuator Workshop* (Hilton Head, SC).
- [48] Van de Pol F C M, van Lintel H T G, Elwenspoek M and Fluitman J H J 1990 A thermopneumatic micropump based on micro-engineering techniques *Sensors Actuators A* **21** 198–202.
- [49] Tsai J H and Lin L 2002 A thermal-bubble-actuated micronozzle-diffuser pump *J. Microelectromech. Syst.* **11** 665–71.
- [50] Rapp R, Schomburg W K, Maas D, Schulz J and Stark W 1994 LIGA micropump for gases and liquids *Sensors Actuators A* **40** 57–61.
- [51] Bohm S, Olthuis W and Bergveld P 1999 A plastic micropump constructed with conventional techniques and materials *Sensors Actuators A* **77** 223–8.
- [52] Yun K-S, Cho I-J, Bu J-U, Kim C-J and Yoon E 2002 A surface-tension driven micropump for low-voltage and low-power operations *J. Microelectromech. Syst.* **11** 454–61.
- [53] B. D. Iverson and S. V. Garimella, “Recent advances in microscale pumping technologies: A review and evaluation,” *Microfluid. Nanofluid.*, vol. 5, no. 2, pp. 145–174, 2008.
- [54] D. A. LaVan, T. McGuire, and R. Langer, “Small-scale systems for in vivo drug delivery,” *Nat. Biotechnol.*, vol. 21, no. 10, pp. 1184–1191, Oct. 2003.
- [55] T. Bourouinay, A. Bosseboeuf, and J. P. Grandchamp, “Design and simulation of an electrostatic micropump for drug-delivery applications,” *J. Micromech. Microeng.*, vol. 7, no. 3, pp. 186–188, Sep. 1997.
- [56] S. Z. Razzackia, P. K. Thwara, Y. G. Ming, V. M. Ugazb, and M. A. Burnsa, “Integrated microsystems for controlled drug delivery,” *Adv. Drug Del. Rev.*, vol. 56, no. 2, pp. 185–198, Feb. 2004.
- [57] D. Maillefer, S. Gamper, B. Frehner, and P. Balmer, “A high-performance silicon micropump for disposable drug delivery systems,” in *Proc. 14th IEEE Int. Conf. MEMS*,

- 2001, pp. 413–417. su and pidaparti: drug particle delivery investigation through a valveless micropump 1399.
- [58] M. Teymoor and A. S. Ebrahim, “Design and simulation of a novel electrostatic peristaltic micromachined pump for drug delivery applications,” *Sens. Actuators A, Phys.*, vol. 117, no. 2, pp. 222–229, Jan. 2005.
- [59] R. Shawgo, S. Richards, A. C. Grayson, Y. W. Li, and M. J. Cima, “BioMEMs for drug delivery,” *Current Opinion Solid State Mater. Sci.*, vol. 6, no. 4, pp. 329–334, Aug. 2002.
- [60] F. E. Tay, *Microfluidics and BioMEMS Application*. Norwell, MA: Kluwer, 2002.
- [61] J. G. Smits, “Piezoelectric micropump with three valves working peristaltically,” *Sens. Actuators A, Phys.*, vol. 21, no. 1–3, pp. 203–206, Feb. 1990.
- [62] H. T. G. van Lintel, “A piezoelectric micropump based on micromachining of silicon,” *Sens. Actuators*, vol. 15, no. 2, pp. 153–167, Oct. 1988.
- [63] W. L. Benard, H. Kahn, A. H. Heuer, and A. Huff, “Thin-film shapememory alloy actuated micropumps,” *J. Microelectromech. Syst.*, vol. 7, no. 2, pp. 245–251, Jun. 1998.
- [64] C. Yamahata, C. Lotto, E. Al-Assaf, and M. A. M. Gijs, “A PMMA valveless micropump using electromagnetic actuation,” *Microfluid. Nanofluid.*, vol. 1, no. 3, pp. 197–207, Jul. 2005.
- [65] A. T. Al-Halhouli, A. Al-Salaymeh, M. I. Kilani, and S. Buttgenbach, “Numerical investigation of the effect of spiral curvature on the flow field in a spiral channel viscous micropump,” *Microfluid. Nanofluid.*, vol. 3, no. 5, pp. 537–546, Oct. 2007.
- [66] S. Z. Qian, A. H. Wang, and J. K. Afonien, “Electrophoretic motion of a spherical particle in a converging–diverging nanotube,” *J. Colloid Interface Sci.*, vol. 303, no. 2, pp. 579–592, Nov. 2006.
- [67] D. W. Trahan and P. S. Doyle, “Simulation of electrophoretic stretching of DNA in a microcontraction using an obstacle array for conformational preconditioning,” *Biomicrofluidics*, vol. 3, no. 1, p. 012803, Mar. 2009.
- [68] M. Nabavi, “Steady and unsteady flow analysis in microdiffusers and micropumps: A critical review,” *Microfluid. Nanofluid.*, vol. 7, no. 5, pp. 599–619, Nov. 2009.
- [69] I. Eames, A. Azarbadegan, and M. Zangeneh, “Analytical model of valveless micropumps,” *J. Microelectromech. Syst.*, vol. 18, no. 4, pp. 878–883, Aug. 2009.
- [70] D. B. Weibel and G. M. Whitesides, “Applications of microfluidics in chemical biology,” *Current Opinion Chem. Biol.*, vol. 10, no. 6, pp. 584–591, Dec. 2006.
- [71] F. A. Gomez, *Biological Applications of Microfluidics*. Hoboken, NJ: Wiley-Interscience, 2008.

- [72] D. D. Carlo, D. Irimia, R. G. Tompkins, and M. Toner, "Continuous inertial focusing, ordering, and separation of particles in microchannels," *Proc. Nat. Acad. Sci. U.S.A.*, vol. 104, no. 48, pp. 18 892–18 897, Nov. 2007.
- [73] N. Pamme, "Continuous flow separations in microfluidic devices," *Lab Chip*, vol. 7, no. 12, pp. 1644–1659, Dec. 2007.
- [74] S. Choi, S. Song, C. Choi, and J. K. Park, "Continuous blood cell separation by hydrophoretic filtration," *Lab Chip*, vol. 7, no. 11, pp. 1532–1538, Nov. 2007.
- [75] Y. Ai, S.W. Joo, Y. T. Jiang, X. C. Xuan, and S. Z. Qian, "Pressure-driven transport of particles through a converging-diverging microchannel," *Biomicrofluidics*, vol. 3, no. 2, p. 022404, Jun. 2009.
- [76] K. Koombua, R. M. Pidaparti, and G. M. Atkinson, "Microfluidic simulations of micropump with multiple vibrating membranes," in *Proc. 11th Int. Conf. Model. Simul. Microsyst.*, Boston, MA, 2008, pp. 557–560.
- [77] G. Su and R. M. Pidaparti, "Transport of drug particles in micropumps through novel actuation," *Microsyst. Technol.*, vol. 16, no. 4, pp. 595–606, Apr. 2010.
- [78] H. Zhang, C. H. Chon, X. Pan, and D. Li, "Methods for counting particles in microfluidic applications," *Microfluid. Nanofluid.*, vol. 7, no. 6, pp. 739–749, Dec. 2009.
- [79] S. Saliterman, "Technology & engineering," in *Fundamentals of Bio- MEMS and Medical Microdevices*. Bellingham, WA: SPIE, 2006.
- [80] Drug Particle Delivery Investigation Through a Valveless Micropump Guoguang Su and Ramana M. Pidaparti, *Member, IEEE, Fellow, ASME*, *Journal of Microelectromechanical Systems*, Vol. 19, No. 6, December 2010.
- [81] Optimization design of multi-material micropump using finite element method, Meiling Zhua, Paul Kirbya, Martin Wacklerleb, Markus Herzba, Martin Richterba, *Sensors and Actuators A* 149 (2009) 130–135.
- [82] A novel two-stage backpressure independent micropump: modeling and characterization A Geipel¹, A Doll¹, P Jantschke¹, N Esser¹, U Massing², P Woias¹ and F Goldschmidtboeing¹, *J. Micromech. Microeng.* 17 (2007) 949–959.
- [83] Modeling and characterization of a nanoliter drug-delivery MEMS micropump with circular bossed membrane Tachung C. Yih, PhD,^a T Chiming Wei, MD, PhD,^b Bashar Hammad, PhD, *Nanomedicine: Nanotechnology, Biology, and Medicine* 1 (2005) 164–175.
- [84] Simulation of MEMS Piezoelectric Micropump for Biomedical Applications, Ulises F. Gonzalez, Ph.D, ALGOR, Inc, Walied A. Moussa, Ph.D.
- [85] Droplet formation based on nozzle vibrant technology, Weber .1931.

